Short-Wave Infrared Lidar on Atmospheric Aerosols and Insects

MARIAM ANDERSSON | DEPARTMENT OF PHYSICS | LUND UNIVERSITY

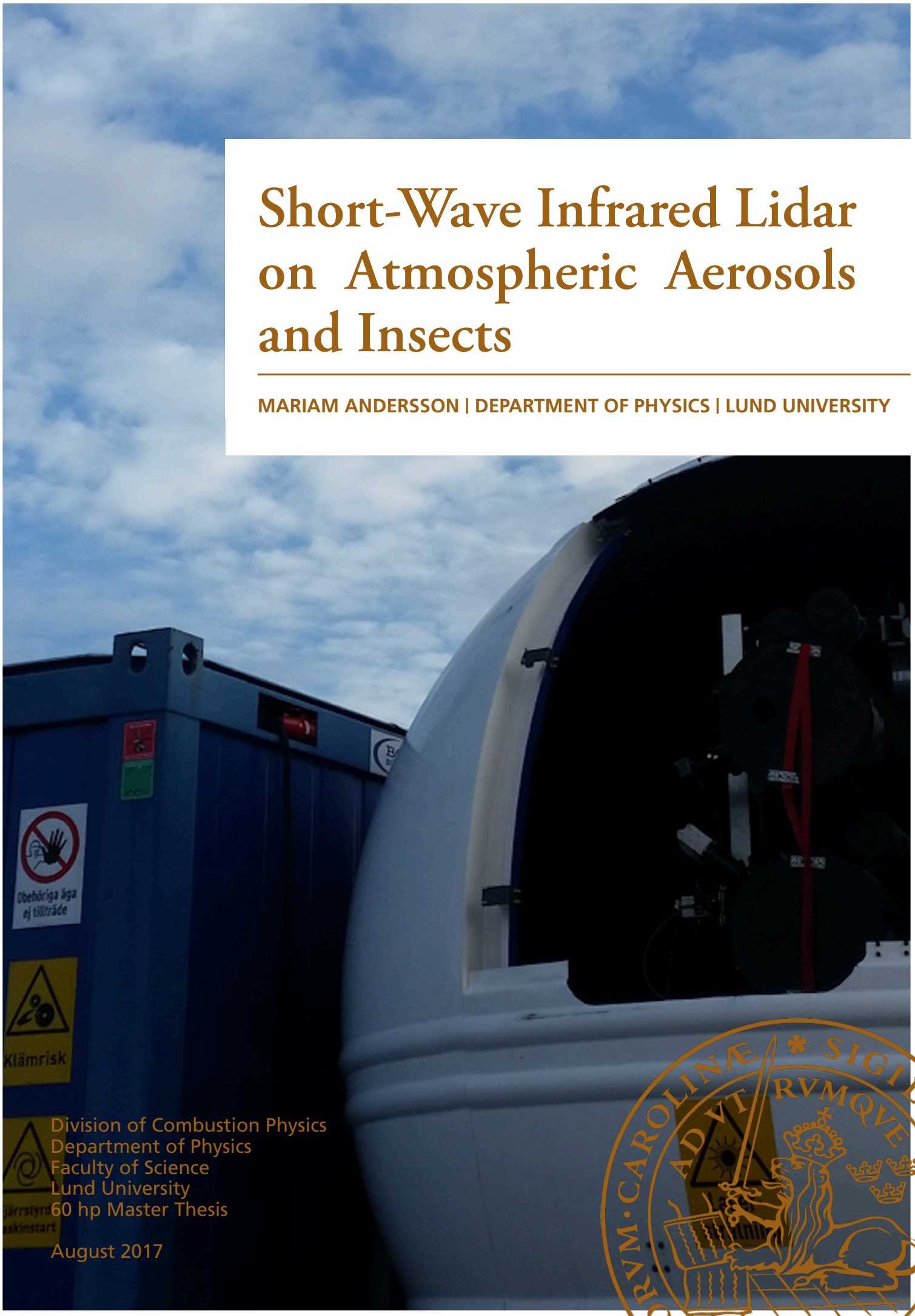

Division of Combustion Physics
Department of Physics
Faculty of Science
Lund University

60 hp Master Thesis

August 2017

Short-Wave Infrared Lidar on Atmospheric Aerosols and Insects

Mariam Andersson

LUND
UNIVERSITY

A Thesis Submitted for the Degree of Master of Science
Supervised by Mikkel Brydegaard, Samuel Jansson and Joakim Bood

Division of Combustion Physics
Department of Physics
Faculty of Science

August 2017

LRCP-206
10th October 2017

Mariam Andersson
Division of Combustion Physics
Department of Physics
Faculty of Science
Lund University
P.O. Box 118
S-221 00 Lund, Sweden

Abstract

This thesis focusses on the implementation of two elastic lidar (light detection and ranging) techniques for the monitoring of atmospheric aerosols and insects at short-wave infrared wavelengths.

Data acquisition software was developed for a time-of-flight system, housed in the Lund University Mobile Biosphere Observatory (LUMBO), with consideration to the intended entomological application. Once up and running, the background signal and noise present in the system was characterised to facilitate future data filtering and background subtraction. The acquisition of a signal from a nearby building was achieved, but revealed that the signal-to-noise ratio of the system was too poor to be able to reliably distinguish any insect events. Attempts to improve the signal-to-noise ratio were made through the construction of a transimpedance amplifier for the receiving avalanche photodiode, but were unsuccessful.

Proof-of-concept dual-band measurements on atmospheric aerosols and insects were performed with a Scheimpflug lidar system. The measurements demonstrated the high spatiotemporal resolution of the system, making possible the localisation and identification of, for example, vehicle emissions. Moreover, it was shown that the ratio between the backscattered signal in the two bands can be used to distinguish between different particle plumes, indicating the potential of the technique to identify aerosols. Furthermore, the dual-band measurements on insects demonstrated the ability of the apparatus to resolve the wing beat frequencies of the organisms in question, along with several associated higher harmonics in the Fourier transform of the time series data.

Contents

List of Abbreviations

ADC Analogue-to-Digital Converter
APD Avalanche Photodiode
BW Bandwidth
CW Continuous Wave
DAQ Data Acquisition
DIAL Differential Absorption Lidar
EMI Electromagnetic Interference
Er:FL Erbium Fibre Laser
FT Fourier Transform
FOV Field of View
GS/s Gigasamples per second
InGaAs Indium Gallium Arsenide
IR Infrared
Lidar Light detection and ranging
LR Line Rate
NIR Near Infrared (0.7-1 μm)
OCS Optical Cross Section
SBR Signal-to-Background Ratio
SDK Software Development Kit
SNR Signal to Noise Ratio
SWIR Short-wave Infrared (1-2.5 μm)
TEC Thermoelectric Cooler
TIA Transimpedance Amplifier
TOF Time-of-flight
UV Ultraviolet
WBF Wing-beat Frequency

Part I

Introduction

Remote sensing is the name given to methods of acquiring and extracting information about a target object or phenomenon from a distance. Human beings perform *passive* remote sensing almost uninterruptedly in the form of vision, hearing and smell to navigate our environment. Early forms of *active* remote sensing techniques are encountered in the animal kingdom with one example evolving around 65-85 million years ago, during the Mesozoic era. The pioneers of these acoustic experiments were bats that used the echoes from their calls to perceive the surrounding environment in complete darkness [1]. Moving forward to the current age, active remote sensing techniques are employed in a multitude of different fields. This thesis focusses on the use of the remote sensing technique Light Detection and Ranging (lidar) on aerosols and aerofauna. Lidar is an active remote sensing technique able to extract information about range and other physical properties of a target from the backscattered light arising from its illumination with light of wavelengths ranging from the infrared (IR) to the ultraviolet (UV).

The first mention of a variation of lidar was in 1930, when E.H. Synge suggested that the density of the atmosphere could be characterised by the scattered light arising from the intersection of a number of light beams in an air volume at a height of up to 30 km [2]. With the invention of the laser in the 1960s, lidar evolved into a powerful optical remote sensing technique, capable of feats ranging from mapping the topography of Mars aboard the Mars Global Surveyor Spacecraft [3] to measuring vegetation densities/types and playing a key role in navigation systems for the rapidly growing field of autonomous vehicles [4].

Probing hard targets such as the surrounding environment in the operation of autonomous vehicles, or terrain surfaces, makes use of the timing at which an emitted laser pulse returns to gather range information. Lidar on volumetric targets that consist of a gaseous distribution of molecules – such as the atmosphere – however, demands the use of lidar systems with superior sensitivity and the registration of not only the timing at which the emitted laser light returns, but also the full-waveform signal strength.

Lidar is mostly applied in topological studies and atmospheric characterisation, and has in the past decade also been adapted for entomological applications.

0.1 Atmospheric Lidar

Climate change is one of the greatest challenges of modern time. Anthropogenic burning of fossil fuels and biomass is a significant contributor to the increase in insulating greenhouse gases and hazardous particles, or aerosols, in the atmosphere [5]. Atmospheric aerosols interact with the solar radiation incident on the Earth, as well as the thermal radiation leaving the Earth's surface, through scattering and absorption processes. In such a way, they play a large role in the net radiation flux to/from Earth, affecting temperature and climate. Moreover, the presence of atmospheric aerosols and pollutants arising from anthropogenic activities are thought to cause 3.3 million premature deaths per year worldwide [6] – it is thus of the utmost importance to be able to quantify and

characterise atmospheric aerosols, as well as locate their sources. Lidar has seen widespread application within this field and is a popular method of gathering height- and temporally-resolved physical and optical data on atmospheric aeorosols over longer periods of time, something which is critical in studies related to the spread of emitted pollution over geographical areas, the formation of precipitation and air quality [7].

In addition to being an invaluable tool in atmospheric and environmental studies, lidar can be used to detect and monitor aero-fauna such as insects and birds in the atmosphere [8, 9]. Remote monitoring of insect movement in the field has previously been performed by means of entomological radar [10, 11]. Harmonic radar methods, for example, have been designed and implemented to track individual insects after having equipped them with miniature transponders [12, 13]. Vertical beam radars, directed up into the atmosphere, can be used to deduce insect physical properties and wing-beat frequency [14]. Lidar systems, however, offer the advantage that the shorter wavelengths used can probe the absorption bands of certain molecules in the optical regime, e.g. water and melanin, to gain richer information about the insect target [15]. Based on wing-beat frequency and optical cross section (OCS), species identification is possible [16]. With sampling rates in the kHz region, distinction between the wing and body cross sections can be made [17]. Remote methods of detecting aero-fauna provide a tool to learn more about insect behaviour in relation to predation, mating and insect group dynamics. Hence, lidar provides a platform for monitoring insect population densities of agricultural pests such as locusts, disease carrying species such as the malaria mosquito and other species that serve as bio-indicators for the health of the local ecosystem [18, 19]. The application of lidar to the identification of aero-fauna is recent and is – to date – mainly being developed by one research group in Lund, Sweden and one in Montana, U.S.A [20, 21, 22, 23].

0.2 Aim

This thesis aims to document efforts in the implementation of two forms of lidar, time-of-flight (TOF) and Scheimpflug lidar, in atmospheric measurements of insects and aerosols respectively using short-wave infrared (SWIR) wavelength laser light.

For the TOF system, a data acquistion process that takes into consideration time, data storage and data quality in terms of spatial resolution and signal to noise ratio (SNR) was developed to ensure that the obtained data would contain as much relevant information as possible to detect insects and deduct their wing beat frequencies (WBFs) at long ranges. The background signal present in the system was characterised and the main sources of disturbances identified to facilitate future background/noise removal or filtering. A photodiode (PD) was constructed to act as an optical trigger for the measurements and, once running, the lasers were directed towards the wall of the nearby chemistry building from which signals were obtained. Attempts were made to further increase the amplitude and SNR of the obtained signal by varying the impedance level on the oscilloscope by which the signal was sampled.

With the Scheimpflug system, proof-of-concept dual band-measurements were performed on particle plumes – particle samples released into the atmosphere – with the intention of investigating the potential of the method in identifying and quantifying aerosols in the SWIR region. With the same intention, dual band insect measurements were performed.

Part II

Theory

1 Lidar Technology

1.1 Time-of-Flight Lidar

TOF lidar is the most commonly implemented lidar technique and utilises pulsed laser light to determine the distance to a scatterer in the probe volume. The round trip time, Δt, at which a backscattered pulse travelling at the speed of light, c, arrives (relative to its emission) at the detector is indicative of the distance, r, between the detector and the point at which the backscatter occurred according to:

$$r = \frac{c\Delta t}{2} \tag{1}$$

The repetition rate, f_{rep}, of the laser puts a constraint on the maximum distance, r_{max} at which an object can be accurately ranged. r_{max} is given by:

$$r_{max} = \frac{c}{2 \cdot f_{rep}} \tag{2}$$

Backscattered light arising from objects outside the bounds of r_{max} will, depending on the timing with which their reflections arrive at the detector, appear to be coming from another point within r_{max}. In order to prevent this, the beam can be terminated at a distance smaller than or equal to r_{max}. The range resolution of the TOF system is limited by three factors: the laser pulse duration, τ; the bandwidth (BW) of the detector; and the frequency at which the signal from the detector is sampled f_s.

1.2 Scheimpflug Lidar

Scheimpflug lidar is a variation of lidar developed at Lund University [8], and is based on the Scheimpflug principle [24]. In contrast to TOF lidar, it makes use of inexpensive continuous-wave (CW) laser sources and range information is obtained from backscattered light through the geometrical arrangement of the detector, the lens and the object plane (laser beam) as shown in Figure 1.

In most detector-lens arrangements, the lens plane is parallel to the image plane. The tilting of the detector array with respect to the lens plane in Figure 1, however, associates each pixel of the array with a range interval. The spatial precision with which a signal can be traced back to a specific volume along the beam is determined by the distance between the Scheimpflug system and the

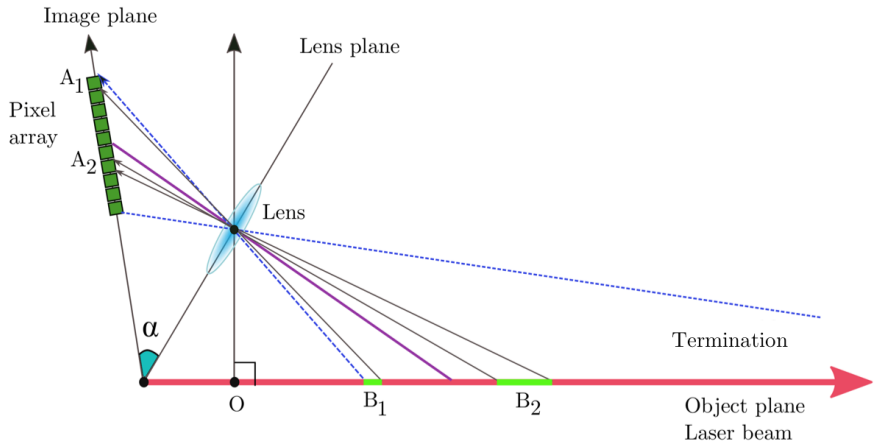

Figure 1: *Schematic of the Scheimpflug lidar setup. The detector plane is tilted at an angle α with respect to the lens plane. This arrangement gives focus along the whole laser beam, from a near-field limit, represented by the intersection of the dotted line from A_1 with the laser beam, to the point at which the beam is terminated. In some applications, the beam can be imaged to infinity instead of being terminated. Range information is obtained from the location of the incident signal on the array.*

origin of the signal. Beginning with A_1 in Figure 1, each consecutive pixel images larger range segments i.e. pixel A_1 images the range segment denoted by B_1 and pixel A_2 images a larger range segment B_2. This is exemplified in Figure 2, which shows the ranges corresponding to each pixel in the Scheimpflug lidar arrangement used for this thesis work.

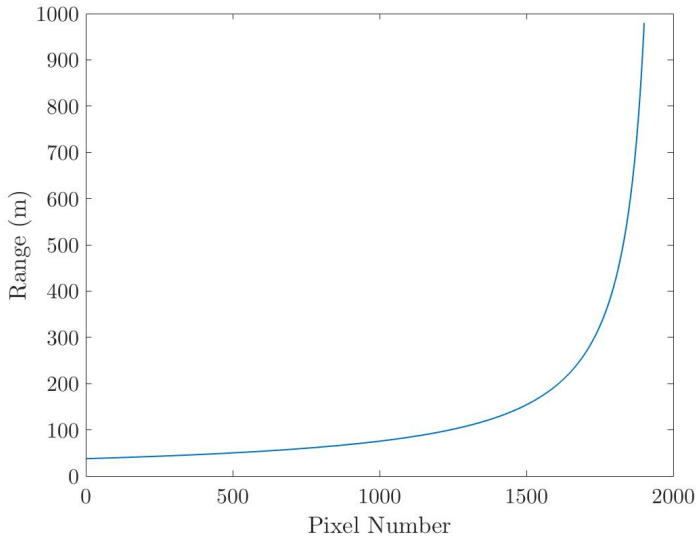

Figure 2: *Variation of range interval measured with pixel number when the Scheimpflug setup at Lund University is calibrated for measurements with a termination at a distance of 980 m.*

The geometrical calculations that are performed to map each pixel in the detector array to a certain range require that the distance to the termination is known.

1.3 Comparison

Entomological Time-of-Flight measurements have previously been performed by a group at Montana State University that has succeeded in acquiring backscattered signals from bees at a range of approximately 100 m [22]. At Lund University, infrastructure to perform TOF measurements exists in the form of the Lund University Mobile Biosphere Observatory (LUMBO). Some specifications of these systems, along with the Lund University Scheimpflug system, are listed in Table 1 for comparison purposes.

Table 1: *Comparison of instrumental specifications of the lidar systems at Lund University and Montana State University [22, 23, 25].*

Specification	**Montana Group**	**LUMBO**	**LU Scheimpflug**
Lidar Technique	TOF	TOF	Scheimpflug
Range Resolution	Constant	Constant	Decays with inverse square of range
Signal Intensity	Decays with inverse square of range	Decays with inverse square of range	Constant for volumetric targets, decays with inverse square of range for hard targets
Wavelength, (nm) λ	532	1550	980, 1550
Pulse Energy (µJ)	>10	150	23,38
Pulse Duration (ns)	<1	6	$90 \cdot 10^3$
Laser Average Power (W)	0.07	3	2.5, 4.2
Repetition/Line Rate (kHz)	7.2	20	10
Receiver Diameter (mm)	152	305	200
Detector Type	Photomultiplier tube	InGaAs avalanche photodetector	InGaAs pixel array
Detector Bandwidth (MHz)	200	113	20.5

The core differences between TOF and Scheimpflug systems lie in the factors that affect: spatial resolution, signal intensity and temporal resolution.

TOF lidar systems are limited in both spatial and temporal resolution by the pulse length, as discussed in Section 1.1. Pulsed laser systems are subject to a ”minimum-duration bandwidth product”, which places a minimum limit on the pulse length proportional to the inverse of the laser BW [26]. This sets an intrinsic limit on the spatial resolution of any TOF system. On the contrary, the spatial resolution of Scheimpflug systems is limited by the pixel size, the detector-target distance (Figure 2) and the quality of the optics used. Further factors that affect the temporal resolution in TOF systems are: pulse repetition rate, detector BW, BW of the analogue-to-digital converter (ADC). Since it is important that pulses do not overlap, the maximum round trip time of the pulse plays a part in deciding the pulse repetition rate. For the Scheimpflug systems, temporal resolution is limited only by the read-out rate of the detector. Lastly, the signal intensity decays with the inverse square of the range in TOF systems, whereas it remains constant in Scheimpflug systems – this gives Scheimpflug the additional ability to constantly measure the atmospheric background signal.

Comparing the LUMBO and Montana TOF systems with each other, it is postulated that the LUMBO system could potentially offer an improvement of either measurement range or minimum

detectable size of atmospheric aero-fauna. The increased range and detection ability is owing to the larger pulse energy, increased pulse repetition rate and receiver diameter. Moreover, the laser wavelength of 1550 nm offers an advantage compared to that at 532 nm; this will be discussed in Section 5.

2 Optical Processes

The interaction between electromagnetic waves and matter occurs in the form of scattering, absorption and emission processes. Scattering occurs when molecules are exposed to radiation, which they subsequently re-radiate in many directions. Scattering processes in which the kinetic energy of the incident photons is conserved are said to be elastic; the wavelength of the scattered radiation is the same as that of the incident radiation. Such a process is depicted in Figure 3.

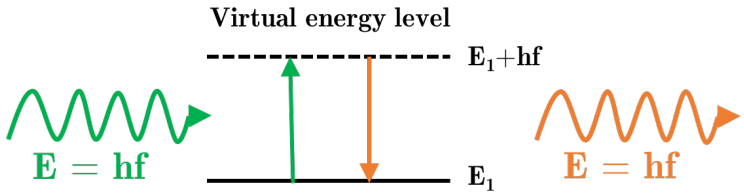

Figure 3: *A quantum mechanical representation of the elastic process of Rayleigh scattering in which the molecule/system is excited by the incident radiation of energy $E = hf$ from state E_1 to a virtual state corresponding to energy $E_1 + hf$. f is the radiation frequency and h is the Planck constant. The radiation is re-emitted upon de-excitation..*

The virtual energy level shown in Figure 3, $E_1 + hf$, is only allowed within the limits of the Heisenberg uncertainty principle and therefore has an extremely short lifetime. Rayleigh scattering occurs when the radiation incident on a target is of a wavelength much larger than the target itself, and the scattering is often in a dipole-antenna pattern. When the target diameter approaches or exceeds the radiation wavelength, this approximation is no longer adequate and scattering occurs preferentially in one direction; Mie scattering is said to occur. These scenarios are depicted in Figure 4.

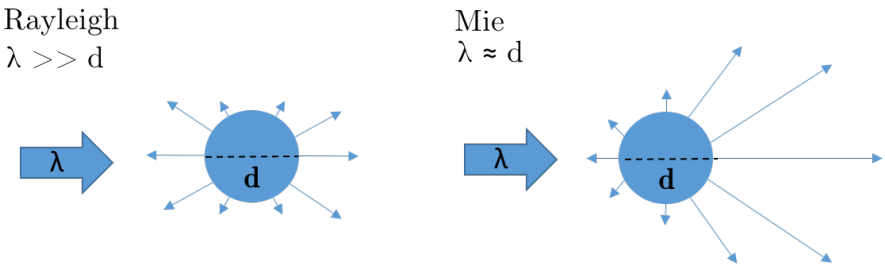

Figure 4: *Rayleigh scattering occurs when the incident radiation is of a wavelength λ much larger than the particle diameter, d. Mie scattering occurs when d approaches, or becomes larger than, λ in size. The angular emission of the incident radiation differs between the two scenarios.*

Moreover, the intensity of the scattered radiation varies with wavelength. For Rayleigh scattering, the intensity of the scattered radiation from a particle of diameter d is proportional to the inverse

fourth power of the wavelength, λ^{-4}. On the other hand, Mie scattering displays an approximate λ^{-2} intensity dependence [27].

Absorption occurs when the incident electromagnetic energy, instead of being re-radiated as electromagnetic energy, is transformed into other energy forms i.e. thermal energy. The proportion of light scattered versus that absorbed is determined by the properties of the medium upon which radiation is incident; the medium properties can be characterised through σ, μ and χ, otherwise termed the phenomenological constants, which represent the conductivity, permeability and electric susceptibility respectively. The phenomenological constants are taken to be frequency-dependent and can have complex values; the imaginary component of these constants is what contributes to absorption processes in the medium [28]. The complex index of refraction, n, can ultimately be traced back to these phenomenological constants and serves as a description of the light propagation through a medium. It can be written:

$$n = n' + n'' \cdot i \tag{3}$$

n' represents the real component of the complex index of refraction and accounts for the refraction, or bending, of light in the medium; this includes reflection at interfaces between media of different refractive indices, governed by the Fresnel equations [29]. In fact, Mie scattering can be regarded as a consequence of the Fresnel equations governing surface reflections:

$$R_s = \left| \frac{n_i \cos\theta_i - n_t \sqrt{1 - (\frac{n_i}{n_t} \sin\theta_i)^2}}{n_i \cos\theta_i + n_t \sqrt{1 - (\frac{n_i}{n_t} \sin\theta_i)^2}} \right|^2 \tag{4}$$

$$R_p = \left| \frac{n_i \sqrt{1 - (\frac{n_i}{n_t} \sin\theta_i)^2} - n_t \cos\theta_i}{n_i \sqrt{1 - (\frac{n_i}{n_t} \sin\theta_i)^2} + n_t \cos\theta_i} \right|^2 \tag{5}$$

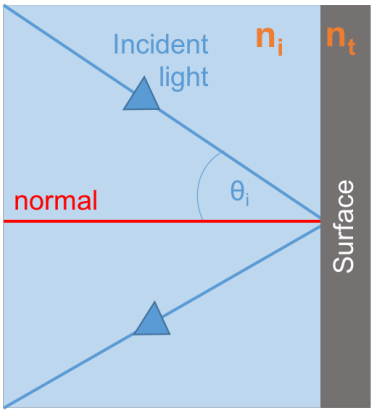

Figure 5: *Fresnel reflection at a surface between two media of differing refractive indices n_i and n_t.*

R_s and R_p represent the reflectance at the interface between the two media for light of perpendicular and parallel polarisation with respect to the plane of incidence respectively. n_i represents the index of refraction in the medium from which the light is incident, whereas n_t is the index of refraction in the medium into which the radiation is transmitted. θ_i is the angle of incidence – the angle between the incident radiation and the normal to the boundary interface between the media. The imaginary component, n'', accounts for the attenuation inside the medium which can be quantified by the absorption coefficient, μ_a. The Beer-Lambert law relates the fraction of internally transmitted light, T, through a substance of length l to μ_a by:

$$T = e^{-\mu_a l} \tag{6}$$

It can be shown that the real and imaginary components of the phenomenological constants are related to each other by mathematical relations called Kramers-Kronig relations and are thus by no means independent of each other [28]. Hence, n' and μ_a are related to each other in the same fashion. Figure 6 shows the spectral variation of μ_a for water vapour and liquid water, along with the spectral variation of refractive index for liquid water.

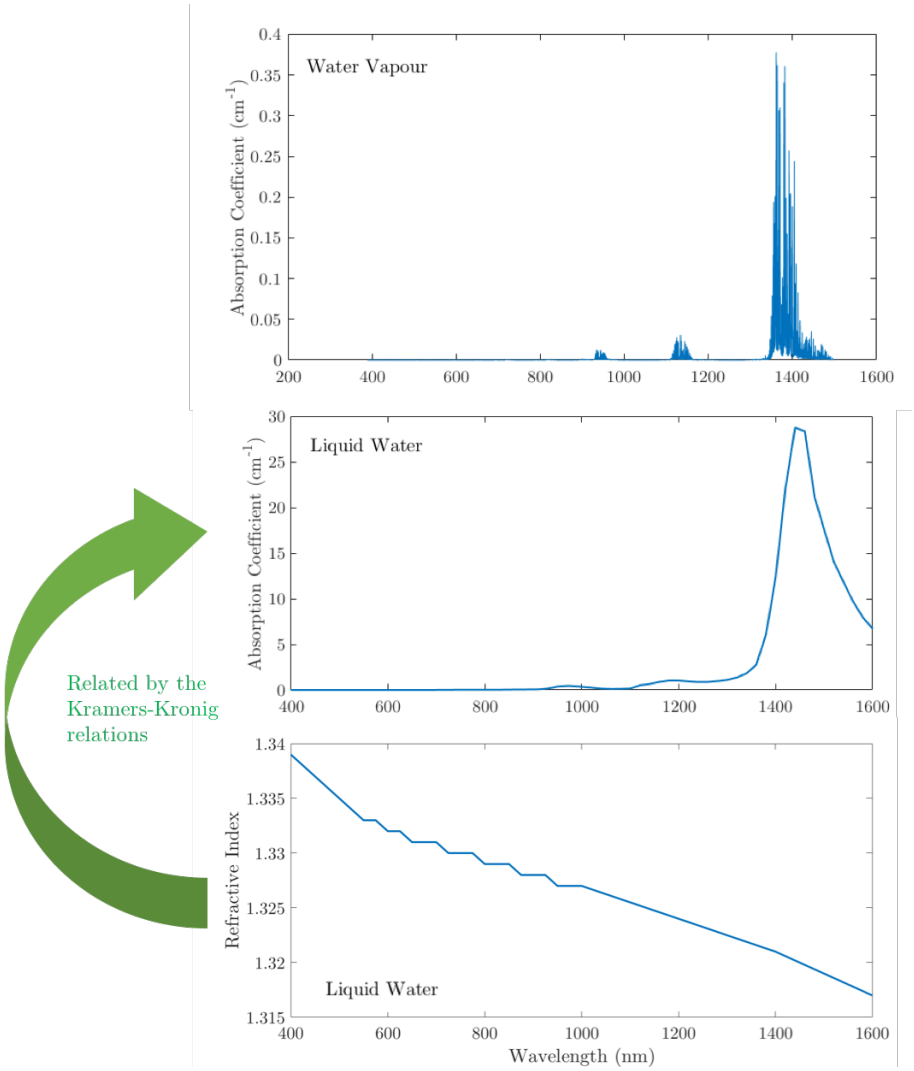

Figure 6: *The absorption spectra of water vapour at atmospheric pressure and liquid water, as well as the spectral variation of refractive index in liquid water. The absorption coefficient and refractive index are related to each other by the Kramers-Kronig relations. Data from [30] and the online HITRAN database [31].*

As seen in Figure 6, the absorption spectrum for water in gaseous form is more complex and intricate than that for water in liquid form, which conveys a smooth absorption across wavelengths. The differences between these spectra are relevant to take into account when considering the absorption that occurs in living insects with a high liquid water content, for example, and the scattering from atmospheric water vapour.

3 Single Mie Scattering in Aerosols

Light scattering from particles suspended in the air, aerosols, can to a certain extent be described by Mie scattering [32]. As mentioned previously, Mie scattering is the process by which light scatters elastically from particles with diameters of similar size to, or larger than, its wavelength. This interaction of light with matter, as illustrated in Figure 7, is described by the Mie solution to the Maxwell Equations. It should be noted that while the Mie solution to the Maxwell equations assumes spherically symmetrical solutions – a far cry from the irregular shapes of many aeorosols – it does give some approximation of what can be expected.

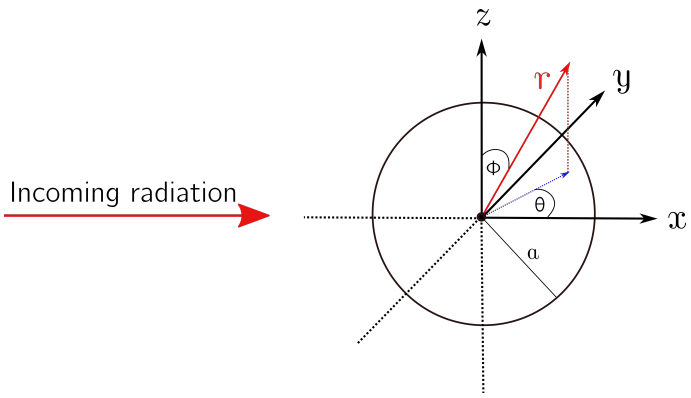

Figure 7: *Interaction of particle with incident radiation. The scattered light is described in spherical coordinates r, Θ, Φ, centred on a spherical particle of radius a.*

The intensity of the scattered radiation varies with angle (θ and ϕ in Figure 7) and polarisation of the scattered light. Mie theory can be applied in order to predict how a light-particle interaction will appear, and what can be expected in terms of backscattered radiation which is what is measured with lidar techniques. To illustrate, MATLAB code developed by Christian Mätzler [33] is used to demonstrate the scattering from a collection of spherical particles with a user-defined complex refractive index. The complex refractive indices of water at different wavelengths, required for the calculations, are obtained from [30].

Figure 8 illustrates the variation of scattering intensity with scattering angle for light of wavelengths 980 nm and 1550 nm incident on a monodisperse volume of water particles.

From Figure 8, it is clear that forward scattering becomes strongly preferential compared to back scattering the more the particle diameter approaches the wavelength of the incident radiation, with this combination of particle diameters and radiation wavelengths. Aerosols are typically not restricted to particles of a single diameter, and it is relevant to consider volumes of polydisperse particles. Examining the relative intensities of the backscattered radiation (at direction 180 °) at a continuum of wavelengths for four different collections of polydisperse particles results in Figure 9.

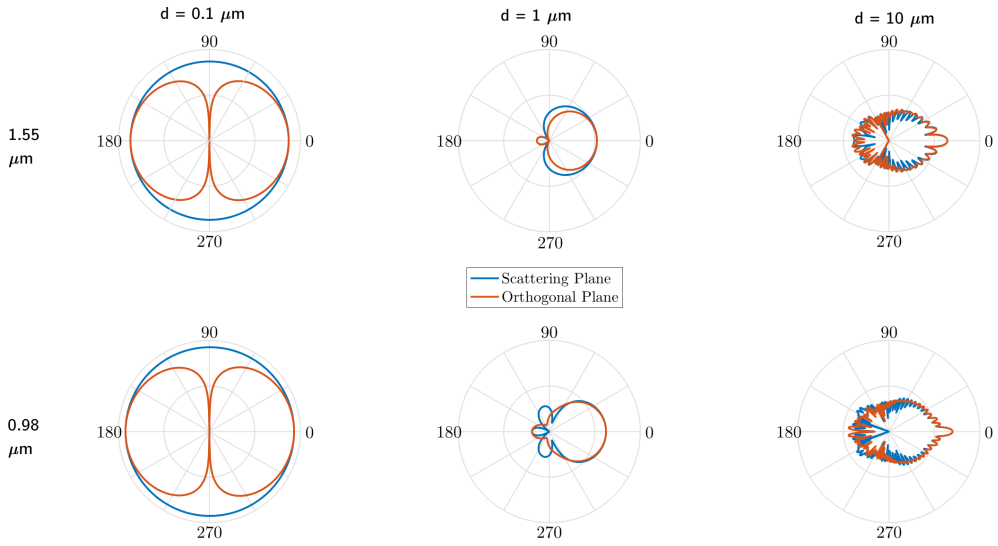

Figure 8: *Relative variation of scattering intensity with scattering angle for light of 980 nm and 1550 nm wavelength incident on a monodisperse volume of water particles from the* $180°$ *direction. Three water particle diameters – 0.1* μm*, 1* μm *and 10* μm *– were simulated. To better illustrate the Mie angular scattering patterns that arise, the polar plots are normalised and logarithmic; the relative differences in backscattered intensities between the different particle diameters is depicted in Figure 9.*

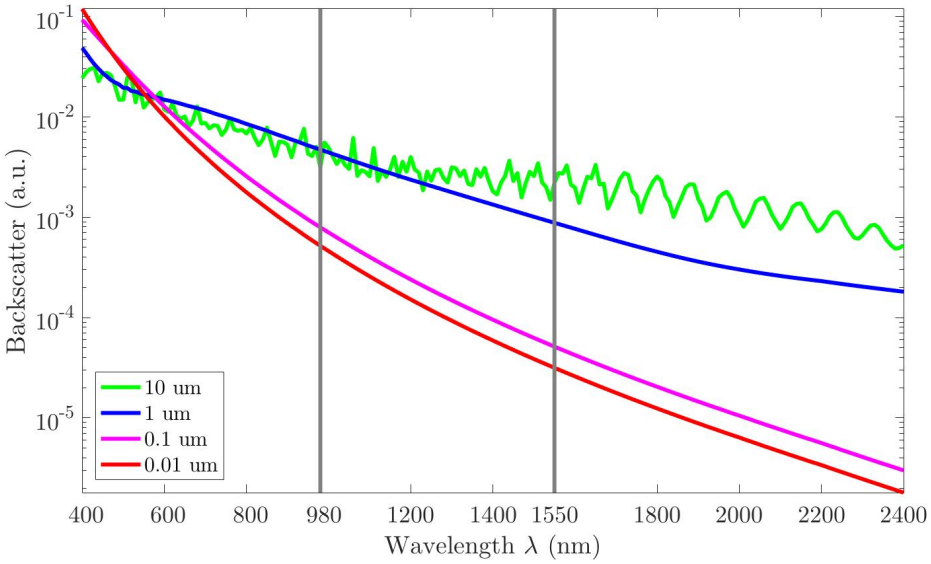

Figure 9: *Relative variation in intensity of backscattered (scattering direction* $180°$*) light from polydisperse collections of water particles with wavelength. The results for four water particle diameters – 0.01* μm*, 0.1* μm*, 1* μm *and 10* μm *– are displayed. The wavelengths 980 nm and 1550 nm are marked for clarity and comparison with Figure 8.*

In Figure 9 the fluctuation of the backscattered intensity at the relatively large particle diameter, 10

μm, compared to the wavelengths, can be attributed to the uncertainties involved in the numerical computation of the backscattered radiation. It is nonetheless clear that the larger the particle, the greater the intensity of the backscattered light. In the atmosphere, Mie scattering from particles is more significant in comparison to the Rayleigh scattering occuring from molecules [27]. As discussed in Section 2, particles that have significantly smaller diameters than that of the incident radiation will Rayleigh scatter almost equally in all directions with a wavelength dependency of λ^{-4} while those with diameters comparable to the wavelength in question will roughly adhere to a λ^{-2} dependence. The intensity of the scattered radiation is quantified by the scattering coefficient, μ_s.

Hitherto, a brief outline of the angular and spectral nature of single Mie scattering from aerosols has been given. What about the temporal characteristics of scattering, given that the particles are in motion? Experiments in clear, foggy and snowy weather conditions were performed with the Scheimpflug technique described in Section 1.2 at a wavelength of 1550 nm. Figure 10 show the varying frequency content of the atmospheric signal at different distances for the three atmospheric conditions.

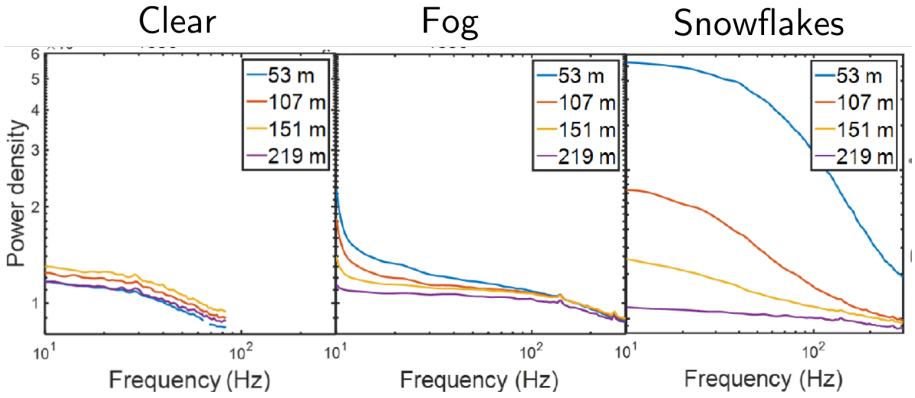

Figure 10: *Variation of frequency content of backscattered atmospheric signal at four different ranges during three atmospheric conditions: clear, foggy, snowy. Measurements were performed with a Scheimpflug apparatus at a wavelength of 1550 nm. Exposure times were normalised to 1 ms. The clear air gives a static signal across the frequency range whereas the foggy and snowy signals skew the frequency distribution. Resolution is higher at shorter ranges. Plots taken from [34].*

The clear air in Figure 10 gives a static signal across the frequency range along all ranges. With the emergence of fog, the measurements at shorter ranges such as 53 m depict a somewhat skewed frequency distribution in comparison to that obtained in clear conditions. As the spatial resolution of the lidar system deteriorates with increasing range, the fog is better resolved at shorter ranges. Hence, at short ranges the fog enters the probe volume, is resolved, and contributes to the low-frequency content of the signal. The sparsely distributed snowflakes, on the other hand, move quickly and contribute towards the higher-frequency end of the spectrum. Again, the contribution is only visible when the snowflakes are spatially resolved by the instrumentation at short ranges. This illustrates the varying spatial resolution of the Scheimpflug setup and what can be expected from scattering by atmospheric particles. A collection of fine particles e.g. water particles in fog are not individually resolved and their movement thus contributes to a low frequency signal. Larger particles, such as snowflakes, can be individually resolved and contribute to high frequency signals.

3.1 Aerosol Identification

In the context of atmospheric lidar on aerosols, the term 'extinction coefficient' is often used. The extinction coefficient is the sum of the scattering coefficient, μ_s, and the absorption coefficient μ_a; it is a measure of the total intensity reduction of the ballistic light. Inelastic lidar techniques such as Raman lidar are able to extract the atmospheric extinction profiles for chosen gases, probing their concentration [35]. Elastic techniques such as differential abosption lidar (DIAL) make use of laser wavelengths that match the absorption bands of certain molecules to extract similar profiles. Examples of such experiments include monitoring atmospheric oxygen concentration [36] and measuring carbon dioxide concentrations as an indicator for volcanic activity [37]. Elastic techniques can either make use of approximations of atmospheric extinction coefficients to determine aerosol concentration or of polarisation measurements on the backscattered light to determine concentration [35, 38, 39]. The polarisation methods can be also be used to identify aerosol species [40]. Hence, the unique scattering response of an aerosol to light of various wavelengths can be used as a means to identify it.

In Figure 9, water particles of diameter 1 µm backscatter light of wavelength 980 nm much more intensely than light of wavelength 1550 nm. Since each aerosol has unique scattering properties, the ratio between the two intensities can be used as a form of spectral fingerprint to identify the aerosol in question.

4 Multiple Mie Scattering in Aero-Fauna

The Mie scattering arising from the interaction of light with the biological tissue of insects or larger objects in the atmosphere cannot be approximated using a single scattering approach. Instead, multiple Mie scattering in tissue, such as that shown in Figure 11, is considered. The optical properties of tissue are given by the absorption coefficient, μ_a (cm$^-$1), the scattering coefficient μ_s (cm$^-$1), the real refractive index, n', and the scattering function $p(\theta, \phi)$ (sr^{-1}) which describes the direction of scattering in every step as shown in Figure 7. As discussed in Section 2, the imaginary component of the refractive index contributes to the absorption and factors into the absorption coefficient by $\mu_a = \frac{4\pi n''}{\lambda}$. For scattering events that exceed a few different consecutive paths, it is unnecessary to consider the angular scattering distribution in as much detail as that shown in Figure 8 and an anisotropy factor, $g =< \cos\theta >$ is introduced as a measure of the relative forward and backward scattering intensities instead of (θ, ϕ). A common convention is to combine μ_s and g to give the *reduced* scattering coefficient, $\mu_s' = \mu_s(1-g)$[cm^{-1}]. [41]

The attenuation length, l, is the inverse of the absorption coefficient μ_a and specifies the length at which the original intensity of the radiation has decreased by a factor $\frac{1}{e}$ or, in other words, the length at which the probability of a particle not having been absorbed is $\frac{1}{e}$. The total length of the random walks taken by the incident photons in Figure 11 can be scaled linearly according to the scattering coefficient; l_1 is larger than l_2 as a result of the lower scattering coefficient μ_{s1}. Furthermore, an increase in g would elongate the total path length in the direction of the incident radiation. The opposite is true for a decrease in g.

The effect of path length through water on the backscattered signal from a bumblebee is shown in

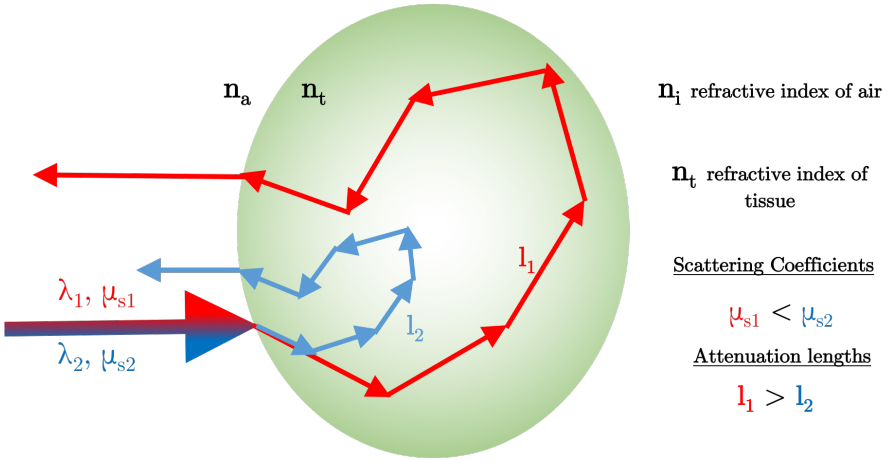

Figure 11: *Schematic of multiple scattering in a medium of refractive index n_t, with scattering coefficients, μ_{s1} and μ_{s2}, and attenuation lengths l_1 and l_2 for wavelengths λ_1 and λ_2. The figure represents a theoretical random walk of a single photon in the tissue. In practice, a statistical distribution of photons is observed.*

Figure 12. The signal from the bumblebee was retrieved from hyperspectral measurements on a dry, dead specimen. In reality, the mass composition of insects is dominated by water, with some insects composed of 60%-70% water [42]. Given the water absorption coefficients at different wavelengths acquired from [30], the effects of the incident radiation travelling different path lengths through the water/living insect are shown.

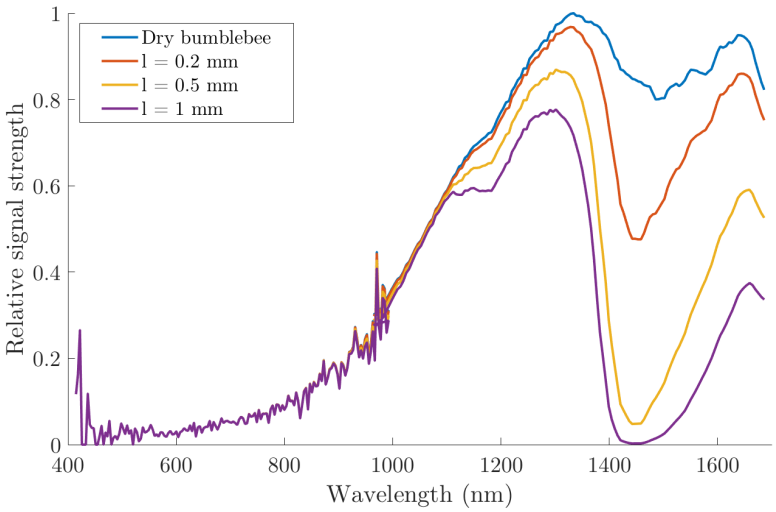

Figure 12: *Variation of the relative strength of the backscattered signal from a bumblebee with wavelength. The blue plot represents the original reflectance spectrum from the dry specimen. For the other spectra, the varying total path lengths through water, l, have been taken into account. Reflectance is depleted at 1550 nm already after a 1 mm path length in the water.*

Examining Figure 12, the strong absorption peak of liquid water around 1450 nm, as shown in Figure 6, becomes more prominent with increasing l. The signals at wavelengths below 1000 nm

are not significantly attenuated.

A temporal variation of the backscattered signal arising from aero-fauna can occur as a result of the beating of the organism's wings and can be used as a species identifier.

4.1 Species Identification

Entomological radar has previously been performed, with radar cross sections for some species determined as a means of identifying them [11]. In the same way, species optical cross sections (OCS) can be established for lidar as a means of species identification.

The OCS for an insect is representative of specimen size and reflectance and describes the area (in two dimensions) that an individual would occupy if it were a non-shiny, diffuse white colour [15]. The challenge posed by using the OCS as a species identifier is that it not only varies between species, but can differ between individuals of the same species and even for the same individual. This comes directly from the fact that an insect can return different signals depending on observation distance, observation angle and phase in the wing-beat cycle. Figure 13 shows an example of the variation of an insect OCS with time.

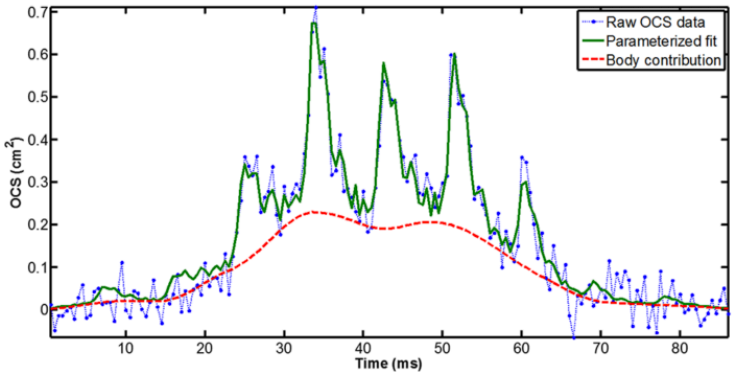

Figure 13: *Example of an insect event at a distance of 1 km, sampled at 2 kHz and wavelength of 808 nm [15].*

The green peaks in Figure 13 are due to specular reflections from the insect wing, whereas the smoother red signal is the contribution from the more diffuse body. From this information, the WBF of the insect can be extracted.

It has been shown that insect echoes can be parametrised by a discrete set of harmonics consisting of the WBF fundamental harmonic and its higher harmonics [43]. As many as 20 higher harmonics have been observed [44]. Hence, the OCS also undergoes oscillation and is described by Equation 7 [15]:

$$OCS(t) = \beta(t) \sum_{h=0}^{h<1/2f_s} (c_{1,h} \sin(2\pi f_0 h t) + c_{2,h} \cos(2\pi f_0 h t)) \tag{7}$$

where t is time, β describes the contribution to the OCS from the insect body, h is the harmonic index, f_s is the sampling frequency, f_0 is the WBF and c denotes OCS coefficients. This parametrisation is a stronger indicator of species than solely the WBF.

The detection of higher harmonics places a requirement on both the detector bandwidth and the frequency at which the signal is sampled – these should be at least twice as large as the frequency of the highest harmonic to be observed in accordance with the Nyquist-Shannon sampling theorem. For insects with typical WBFs around 10-1000 Hz, bandwidths in the kHz regime are required.

5 Spectral Considerations

A high signal-to-background ratio (SBR) allows the detected signal to be discriminated from that of the background. Thus, the reflected signal should be of as high intensity as possible compared to the background signal and noise fluctuations. Selecting lidar wavelengths in spectral regions where the intended target has high reflectance is ideal. Figure 14 shows the relative reflectances of a few different targets.

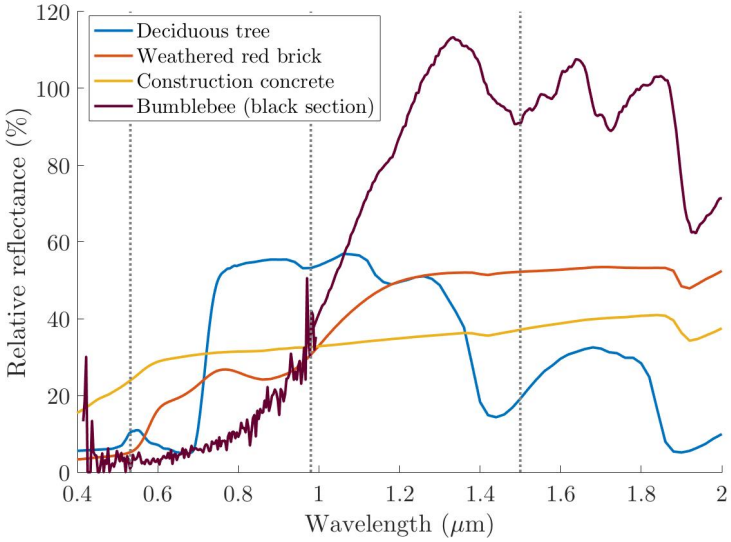

Figure 14: *The variation of relative reflectance with wavelength of different materials/targets. The spectral response of the bumblebee is obtained from hyperspectral measurements while the remaining datasets are sourced from the ASTER library [45]. The wavelengths 532 nm, 980 nm and 1550 nm are marked on the plot. 100% reflectance is defined as that emerging from a diffuse, white surface.*

Probing the bumblebee in Figure 14 at a wavelength of 1550 nm instead of the 532 nm used in the Montana experiments discussed in Section 1.3, gives a significantly stronger backscattered signal provided that the incident radiation is otherwise identical in terms of intensity. However, the low-reflectance absorption lines of gases can also be made use of to probe their atmospheric concentration. Differential absorption lidar (DIAL), for example, involves the use of two wavelengths – one "ON" wavelength on an absorption line and another "OFF" wavelength slightly outside the line – and the differences in the reflected signal to determine concentration i.e. measuring atmospheric

CO_2 around $\lambda = 2000$ nm [46].

Further considerations related to wavelength choice include those regarding solar irradiance and atmospheric attenuation. Figure 15 depicts the spectral solar irradiance on Earth, with and without atmospheric absorption.

Although band-pass, low-pass and high-pass filters can be placed in front of the detector to reduce the background signal originating from ambient light in lidar measurements, solar irradiance at the relevant laser wavelength should be considered. Using lidar wavelengths that correspond to high solar irradiances will lead to increased ambient signal and low SBR. On the other hand, selecting a wavelength within an atmospheric absorption band leads to increased atmospheric attenuation of the laser beam, decreasing SBR at all times of day. There are exceptions to this statement. The fourth harmonic of the Nd:YAG laser at 266 nm exhibits low atmospheric transmission combined with low background levels, owing to the absorption at 266 nm present in the Ozone layer.

Aside from the spectral aspects mentioned above, consideration must be taken to available equipment in the form of light sources and sensors. Keeping in mind that a high SBR is desirable, it follows that high-power lasers and sensors with high quantum efficiency (QE) at the chosen wavelengths are crucial.

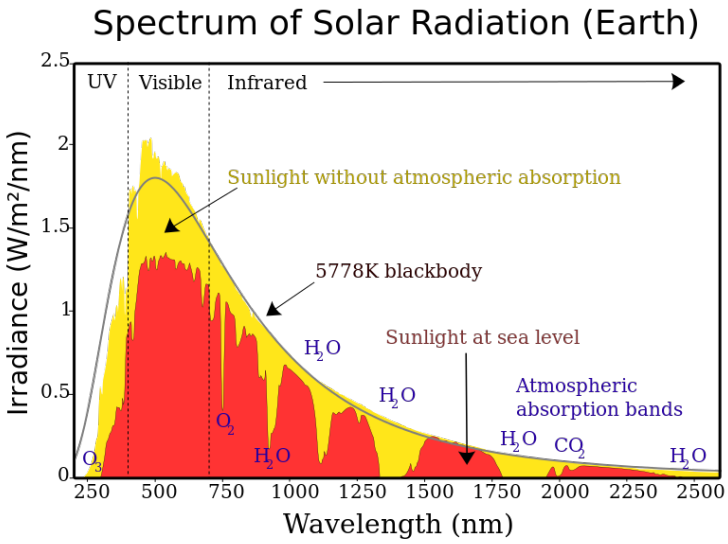

Figure 15: *The spectrum of the solar radiation before and after absorption in the Earth's atmosphere [47].*

6 Temporal Considerations

6.1 Nyquist Frequency

The Nyquist-Shannon sampling theorem defines the minimum discrete sample rate required to reconstruct a continuous signal. It is valid on the condition that the Fourier transform (FT) of the

signal exists within a finite range of frequencies outside which it is zero. The signal is said to have a finite bandwidth. Shannon states the following [48]:

"If a function $f(t)$ contains no frequencies higher than W cps, it is completely determined by giving its coordinates at a series of points spaced $1/2W$ seconds apart."

Here, cps stands for counts per second. In other words, correctly registering a signal requires sampling it at a rate, f_s, at least twice as fast as the frequency of the signal itself. The highest frequency which can be correctly registered at a rate f_s is called the Nyquist frequency, f_N. If sampling occurs below twice the signal frequency, the signal may be incorrectly registered as shown in Figure 16a.

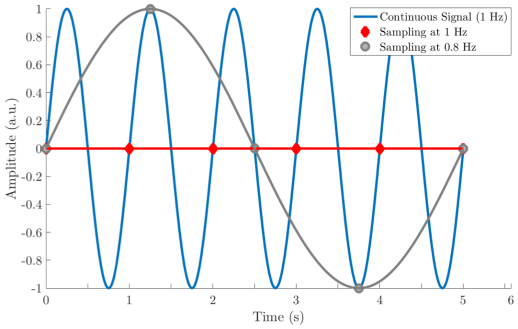

(a)

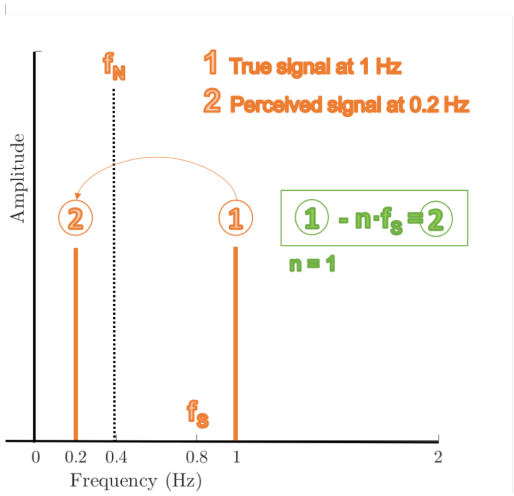

(b)

Figure 16: *a) A 1 Hz sinusoidal signal sampled at 1 Hz registers a constant signal; the same signal sampled at 0.8 Hz gives the appearance of a 0.2 Hz signal. b) A 1 Hz signal sampled at 0.8 Hz appears as a 0.2 Hz signal in the discrete FT of the time series data. Integer multiples (in this case 1) of the sampling frequency are subtracted from the true signal to give aliases appearing below the f_N.*

As Figure 16a shows, a 1 Hz sinusoidal continuous signal sampled at 1 Hz appears as a constant value. If sampling takes place at 0.8 Hz, the resulting signal instead acquires the appearance of a 0.2 Hz sinusoid. In fact, sampling at twice the signal frequency, 2 Hz, may also give rise to a constant-value signal depending on the phase at which measurements take place. In order to

correctly reconstruct the signal, sampling must always take place at frequencies larger than twice the highest frequency of interest [49]. The measurement artifact that occurs when sampling at less than twice f_N, the highest relevant frequency in the signal, is called aliasing. When taking the discrete Fourier transform of the sampled time series to inspect the frequency content of the signal, as in Figure 16b, signals with frequencies higher than the sample rate (f_s) of the measurements will be shifted towards the lower end of the spectrum in f_N, distorting the results.

6.2 Decimation

Decimation is the name given to the process by which a signal undergoes a conversion from a higher sample rate to a lower sample rate. Given a 20 Hz signal, the sample rate can be reduced to 10 Hz by, for example, including only every other data point or by averaging every two points. Oversampling, the process of sampling the signal at a higher sample rate than required, can be used in conjunction with decimation, or downsampling, in order to improve the analogue-to-digital converter (ADC) resolution and reduce noise [50].

The resolution increase scales with the Nyquist frequency,f_N, as follows:

$$f_s = 4^b \cdot f_N \tag{8}$$

where f_s is the sampling frequency required to increase the resolution of the signal by b bits.

Thermal fluctuations, phase noise, quantisation error caused by rounding and truncation and several other sources contribute to the overall noise level present in ADC conversions. The noise is assumed to behave as white noise, having equal intensity at all frequencies. As discussed in Section 6.1, just as any signal at a frequency higher than f_N will be reflected in f_N towards the lower part of the spectrum, so will the noise. The level of this noise is proportional to the inverse square root of the sampling frequency $\frac{1}{\sqrt{f_s}}$ [50]. It follows that the noise in the signal is decreased when the signal is oversampled and subsequently decimated by averaging, and the SNR improves.

A laboratory example of an insect signal and its corresponding power spectrum, displaying the intensity variation of the signal with frequency, are shown in Figure 17.

The WBF of the insect is around 185 Hz, with higher harmonics appearing at multiples of this frequency as described in Section 4.1. Reduction of the original signal in Figure 17a to a sample rate of 1 Hz is performed by both downsampling and averaging to compare the two decimation methods. The resulting power spectra are shown in Figure 18.

The power spectrum in Figure 18a obtained by reducing the original time series to every 20th value is overall noisier than that obtained when averaging every 20 values, seen in Figure 18b. Moreover, more additional peaks seem to arise from aliasing effects in Figure 18a. The peak around 450 Hz present in both power spectra arises from aliasing of the second harmonic around 550 Hz, seen in Figure 17b.

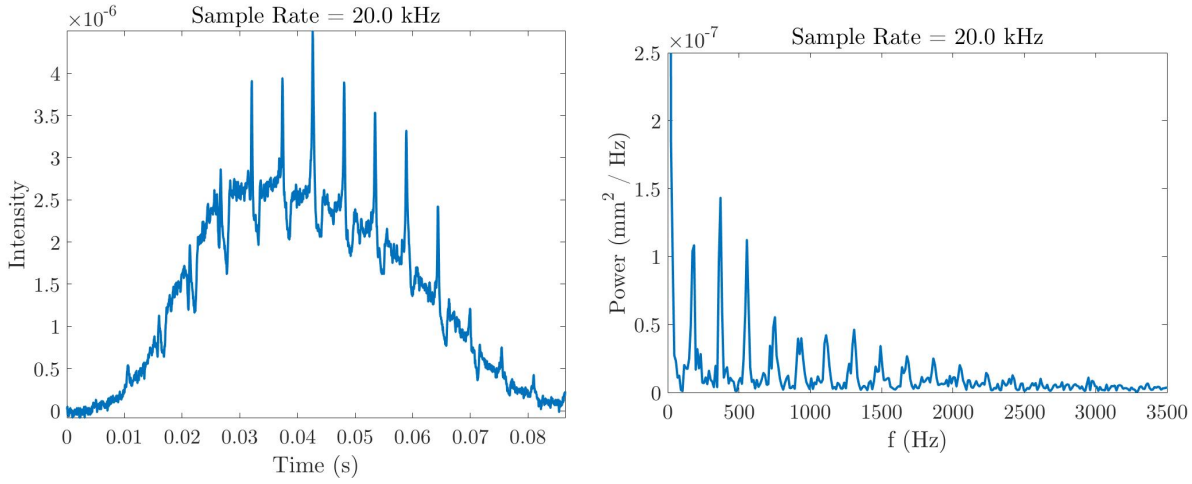

(a) ***(b)***

Figure 17: *Backscattered signal from an insect (Drosophila melanogaster) in a laboratory setting (a), with corresponding power spectrum (b). The signal was measured at a sample rate of 20 kHz and the BW of the detector was 3.5 kHz.*

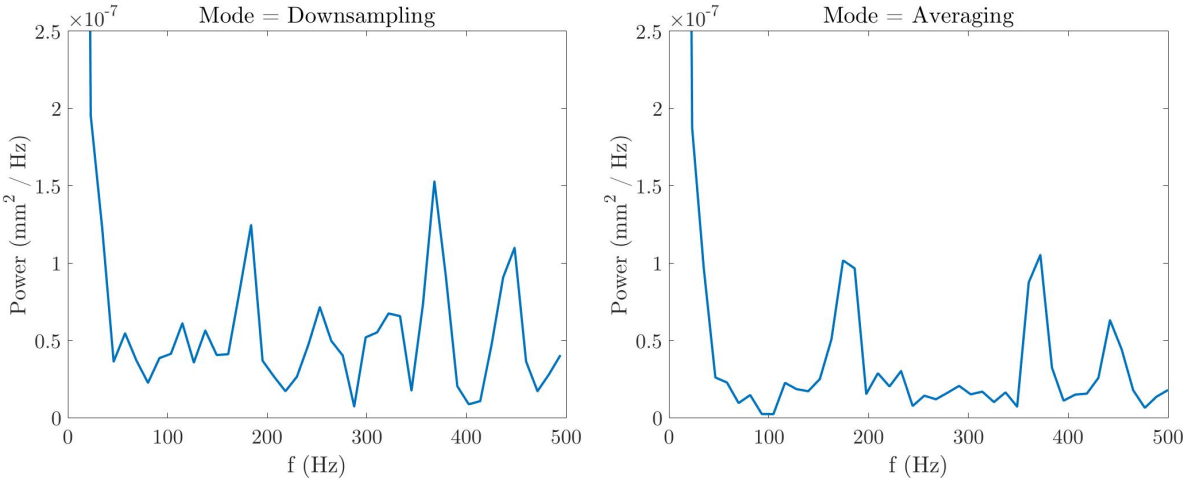

(a) ***(b)***

Figure 18: *Power spectra obtained from the backscattered (Drosophila melanogaster) signal shown in Figure 17. The original 20 kHz signal was reduced to an effective sample rate of 1 kHz by (a) down-sampling, and (b) decimation by averaging.*

Part III

Methods, Results and Discussion

7 Time-of-Flight Lidar

7.1 Experimental Setup and Methods

The LUMBO facility is a reconfigurable mobile facility intended to carry out different types of lidar measurements at a wide range of wavelengths. It is currently stationed on top of the Ecology Department at Lund University shown in Figure 19.

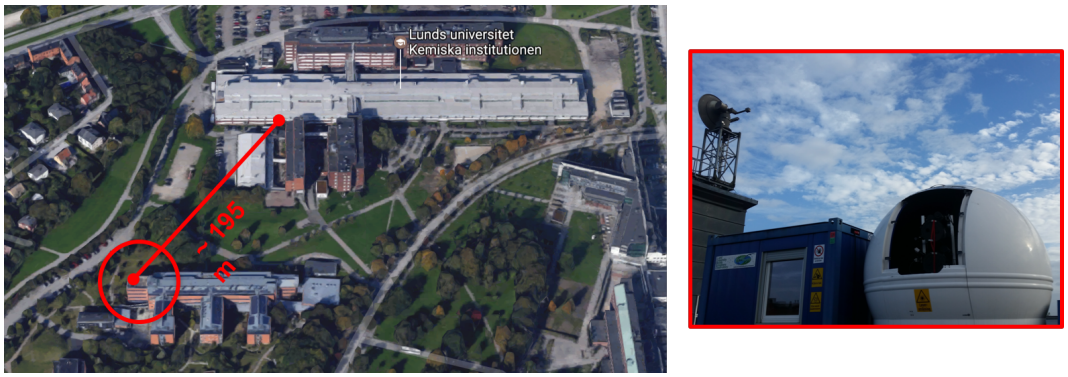

Figure 19: *On left: the red circle marks the current location of LUMBO. On right: LUMBO.*

LUMBO is equipped with a pre-designed TOF system depicted in Figure 20.

The laser source consisted of an Erbium fibre laser (Er:FL) emitting pulses at 1550 nm and a repetition rate of 20 kHz, as controlled by the data acquisition (DAQ) board. A power meter was used to confirm that the average laser power was in the vicinity of the quoted average, 3 W. The 1550 nm laser was overlapped with a pilot beam at 808 nm to monitor the location of termination of the beam. The two laser beams were passed through a beamsplitter which transmitted the 808 nm beam and, to a high degree, reflected the 1550 nm pulses. A small fraction of the 1550 nm beam was transmitted. A photodiode was constructed such that the transmitted 1550 nm signal could serve as an optical trigger (circuit diagram in Appendix A) to the Picoscope 6404D USB oscilloscope. The two beams were then expanded and directed into the atmosphere by a refractor telescope. The x-y mount ensured that the Er:FL position could be adjusted to overlap with the 808 nm beam while the beam divergence was modified by adjusting the focus of the refractor, to ensure that the beam was focussed on the termination. A Newtonian reflector collected the backscattered 1550 nm laser light and imaged it onto an indium gallium arsenide (InGaAs) avalanche photodiode (APD). Upon triggering, the oscilloscope sampled the signal obtained by the APD. Meanwhile, a third refractor telescope imaged the pilot beam onto a Basler camera, sensitive to 808 nm light, with which the beam position could be monitored.

The InGaAs APD had a diameter of 800 µm and was composed of four different segments, each

connected to a BNC cable, allowing the segments to be sampled separately in four different channels. The spatial distribution of the signal across the APD segments of a signal arising from a certain range was indicative of the field of view (FOV) at that point.

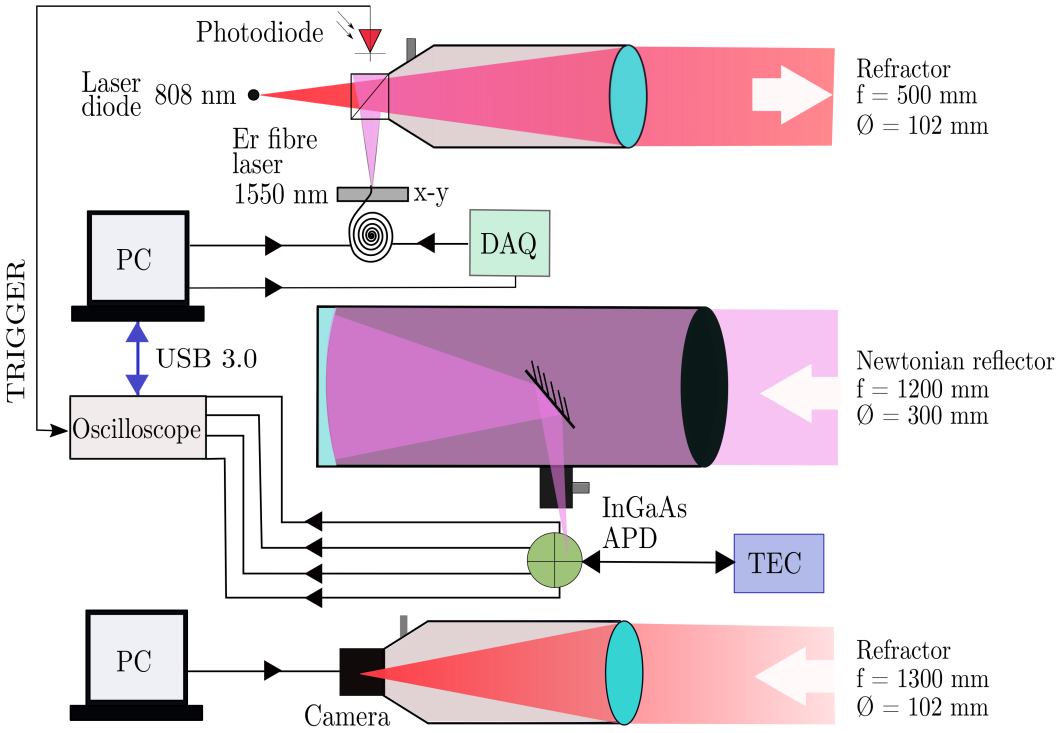

Figure 20: *Schematic showing the TOF system in LUMBO.*

7.1.1 Data Sampling with the Oscilloscope

The InGaAs APD has a BW of 113 MHz and is sampled by a four-channel Picoscope 6404D oscilloscope from Picotech, able to sample at a total maximum rate of 5 gigasamples per second (GS/s) – or, 1.25 GS/s. It has a buffer size of 2 GS where data can be temporarily stored before transfer to a PC.

By writing acquisition software for the oscilloscope in MATLAB with the software development kit (SDK) it can be operated in two ways: streaming mode and rapid block mode. A few different factors shape the ”ideal” acquisition mode in TOF Lidar. One of these is the acquisition time; preferably, the acquisition time should be as long as possible or until the user defines that measurements should stop. At the very least, acquisition time should be on the order of tens of milliseconds to ensure adequate capture of data. For example, the signal from an insect with a WBF of 100 Hz should be sampled for at least 10 ms. Secondly, the sample rate f_s should be sufficiently high so as to retain a high spatial resolution, as mentioned in Section 1.1. High sample rates, however, involve the acquisition and storage of large amounts of data. f_s, therefore, should be high enough to avoid imposing strong constraints on the spatial resolution whilst being as low as possible to minimise the required storage space.

Given these considerations and the specifications of the oscilloscope presented in Table 2, the suit-

ability of the two different methods was assessed.

Table 2: *Specifications for the Picoscope 6404D oscilloscope produced by Pico Tech.*

Picoscope 6404D Specifications	**Value**
Bandwidth	500 MHz
Rise time	3 ns
Resolution	8 bits
Input Range	1 MΩ impedance: ±50 mV to ±20 V in 9 ranges 50 Ω impedance: ±50 mV to ±5 V in 7 ranges
Maximum Sample Rate, 4 Channels	1.25 GS/s (5GS/s for single channel)
Maximum Streaming Rate using SDK (USB 3.0)	156.25 MS/s
Timebase, τ using SDK	0 - 4 (sample interval = $\frac{2^\tau}{5000000}$ 5 - $2^{32}-1$ (sample interval = $\frac{\tau-4}{156250000}$)
Maximum Buffer Segments using SDK	2 000 000
Buffer Memory	2 GS

7.1.2 Alignment and TOF Measurements

Experiments performed at LUMBO involved terminating the beam on the brick wall of the chemistry building approximately 200 m away, North-West of where LUMBO is located in Figure 19.

Alignment of the setup involved three steps: ensuring that the two beams overlapped, ensuring that the 1550 nm beam was focussed on the termination and ensuring that the termination was focussed onto the APD. Overlap was critical in order to control where the 1550 nm beam was targeted, since only the 808 nm beam was visible in the Basler camera and only the 1550 nm beam would induce a signal in the APD. Overlap was obtained by replacing the APD with the Basler camera in the Newtonian reflector and adjusting it such that the 808 nm laser spot on the termination was positioned in the centre of the image obtained. The APD was inserted into the reflector again, and the Er:FL was systematically scanned in the horizontal and vertical direction until a signal was obtained, at which point the two beams were overlapped. Once overlap was attained, focus of the laser beam on the termination was achieved by adjusting the focus of the refractor through which the beam was emitted and monitoring the pilot beam with the Basler camera to minimise its size on the termination. Similarly, achieving focus of the beam onto the APD involved mounting it onto an appropriate length extension tube and adjusting the focus on the Newtonian reflector.

The oscilloscope sampled the APD signal at 1.25 GS/s with an oversampling factor of 10, implying that the effective sample rate was 125 MHz. The data was acquired in blocks of 10 waveforms, consisting of 1000 samples each

7.1.3 Efforts to Improve SNR in Measurements

In an attempt to increase the SNR in the signal from the APD, the impedance level on Channel A from the APD to the oscilloscope was changed by applying an BNC T-connector with resistances higher than that otherwise used (50 Ω). The resistances tested were 150Ω and 270Ω. Lastly, a TIA for the APD was constructed with the aim of increasing the amplitude while maintaining the

APD BW as high as possible. The manufacturer of the APD, Princeton Lightwave, predicted that the APD BW would increase to 203 MHz if a TIA were used. See Appendix B for the frequency response of the APD with/without the TIA and Appendix C for the proposed TIA design.

7.2 Results and Discussion

7.2.1 Developing a Method of Data Acquisition with the Oscilloscope

Streaming Mode

Streaming mode employs a continuous data transfer of the sampled data between the Picoscope and the PC. According to the 6404D specifications, the maximum streaming rate should be 156.25 MS/s shared between the four channels in streaming mode [51]. This entails a streaming rate of approximately 39 MS/s per channel.

It was considered whether or not data transfer between the oscilloscope and the PC could take place at the same time as data sampling as this would be highly advantageous. Figure 21 shows to which degree data can be oversampled for different spatial resolutions and sampling ranges if so is the case.

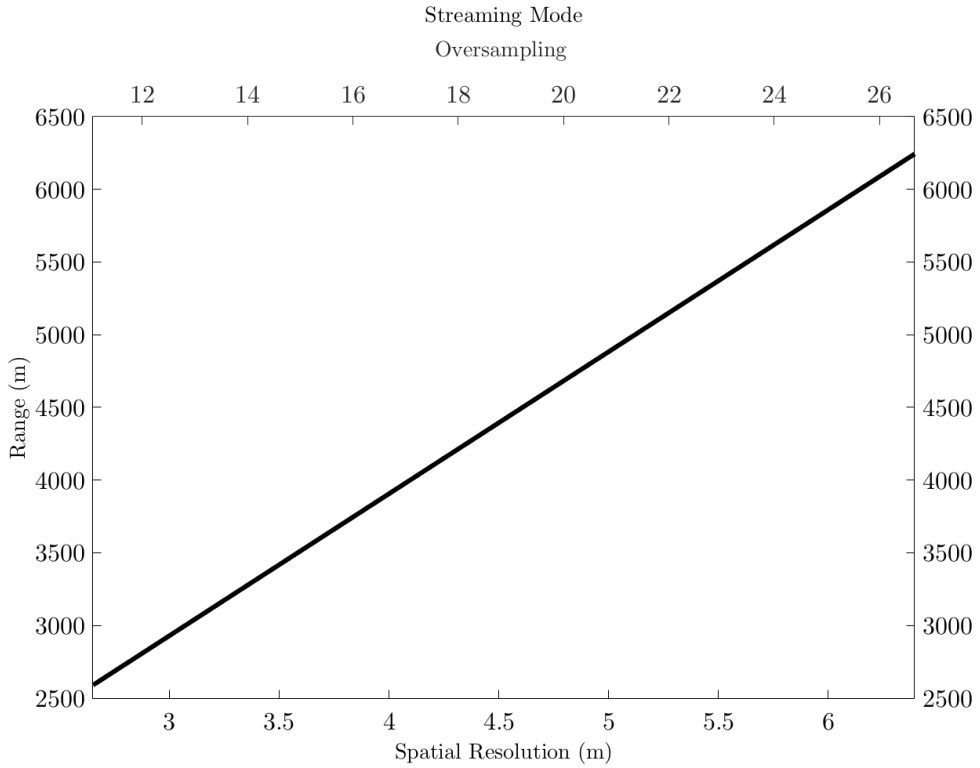

Figure 21: *Plot showing the calculated trade-off between range and spatial resolution when operating the oscilloscope in streaming mode. A 20 kHz pulse rate and sample rate of 1.25 GS/s are assumed. It is also assumed that the data reduction in the oscilloscope takes place continuously by a factor equal to the degree of oversampling shown.*

Figure 21 assumes a 20 kHz pulse repetition rate and a sample rate of 1.25 GS/s per channel, later

to be reduced by the oversampling factor. Also assumed is that sampling of each pulse commences at pulse emission and ceases after the TOF of the laser pulse to the beam termination and back, while data transfer occurs without interruption. Such conditions would be ideal for TOF lidar.

After many attempts, however, it came to light that although the driver functions defined for data sampling and data streaming in streaming mode are separate, they must both run simultaneously and continuously. An implication of this is that the sampling rate, f_s is capped at the maximum streaming rate – 39 MS/s per channel. This sample rate constrains the spatial resolution, x_{res} to 7.68 m by:

$$x_{res} = \frac{2 \cdot c}{2 \cdot f_s}$$

where c is the speed of light.

Oversampling to increase the SNR would impair the spatial resolution further.

Rapid Block Mode

Given a 20 kHz laser pulse repetition rate and a sample rate of 1.25 GS/s, the time taken to fill the buffer at different degrees of oversampling was calculated for a variety of measurement ranges. An 'overhead' of 5 µs where no sampling could take place was assumed to ensure that the oscilloscope would be ready for the next trigger (laser pulse). The results are shown in Figure 22.

Given that one sample is 8 bits (see Table 2), it can be handled by Matlab as an 'int8' signed 8-bit integer and the 2 GS buffer thus translates to 2 GB of data. The PC transfer time shown in Figure 22 refers to the time taken to transfer the 2 GB buffer data to the PC at a rate of 150 MB/s. Above this line, sampling takes place for a longer duration than the data transfer time, while the opposite is true below the line.

After testing the acquisition code in rapid block mode, it became apparent that the downsampling of the signal was not taking place correctly in the oscilloscope . At an oversampling factor n, waveforms of length L were being stored as arrays of the same length on the PC, with the first $\frac{L}{n}$ elements constituting the downsampled signal, and the remainder being zeros. The implication was that neither buffer space nor transfer time were spared. The manufacturer, Pico Technology, was notified and contacted, leading to a modification of the device drivers in order to successfully perform the downsampling in the hardware.

Data acquisition software was written, based on the software examples provided in the SDK. The rough structure of the software is shown in Figure 23.

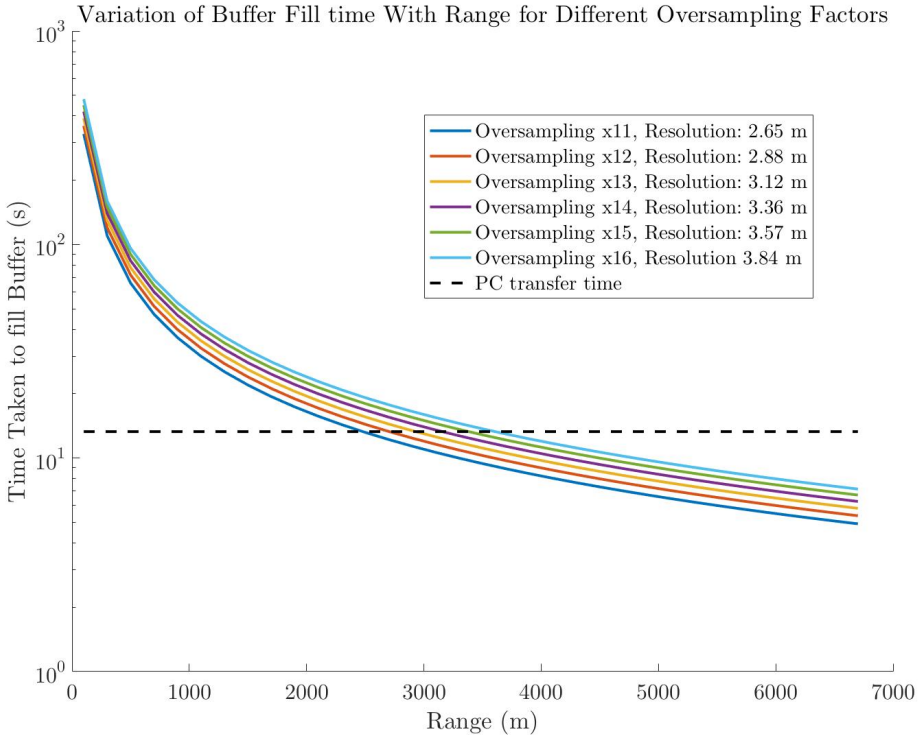

Figure 22: *Variation of time taken to fill the 2 GS Picoscope buffer at a sample rate 1.25 GS/s for varying degrees of oversampling.*

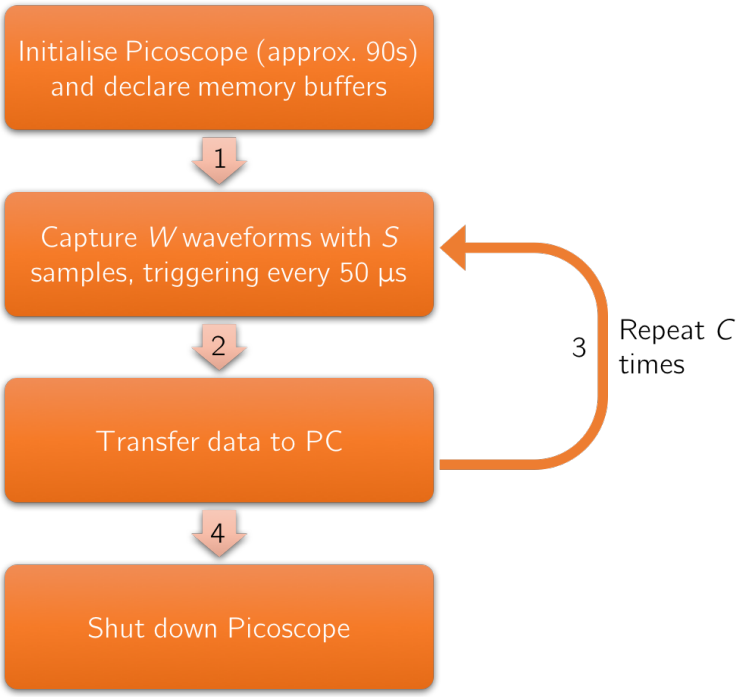

Figure 23: *Rough structure of the* MATLAB *data acquisition script written to sample the avalanche photodiode with the Piscoscope oscilloscope.*

Testing revealed that the acquisition software was slower than expected, to the extent that it would take several hours to fill the buffer and subsequently transfer the data to the PC. In example, the capture and transfer of 10 waveforms with 1000 samples per channel took approximately 300 ms, excluding the time taken to initialise and shut down the oscilloscope. Seeing as there was a 20 kHz trigger, the waveforms should have been captured at 50 µs intervals, meaning that it should take 500 µs in total to sample the signal. A pre-defined function from Pico Tech was used to convert the analogue signal to digital values in the unit mV – this function stored the digital values as double-precision floating point numbers, with a size of 64 bits each [52]. Hence, the total data transferred to and handled by Matlab did not exceed $4 \text{ channels} \cdot 10 \text{ waveforms} \cdot 1000 \text{ samples} \cdot 64 \text{ bits}$, or 640 kB. At a transfer rate of 150 MS/s, the data transfer should take 17.2 ms – an order of magnitude smaller than the measured time.

7.2.2 Noise Characterisation

Previous experiments indicated that the background signal in the TOF system at LUMBO is high, causing periodic disturbances that could be mistaken for, or shroud, the harmonics caused by the modulation from insects' wingbeats. These disturbances manifested as sudden wave packets in the time series data, with distinct features in the frequency domain. In order to characterise the background signal in LUMBO and attempt to determine its source, the signal from the APD was measured in four different scenarios:

1. Cover on receiver telescope (dark), APD not connected to any power supply
2. Cover on receiver telescope (dark), APD connected to 12 V power supply
3. APD exposed to daylight (light), connected to 12 V power supply
4. APD exposed to daylight (light), connected to 12 V battery

Measuring the background signal in these four different scenarios allowed for the effects of optical disturbances, mains disturbances and electromagnetic interference (EMI) to be distinguished from each other.

With knowledge of its Steinhart Hart coefficients, the APD was cooled to -40°C with a thermo-electric cooler (TEC). It was sampled in the scenarios 1) to 4) listed above at a sample rate of 1.25 GHz per channel, giving rise to the power spectra shown in Figure 24.

For comparison purposes, the different data sets in Figure 24 were normalised such that the common peak at 391.6 MHz gave the same contribution for all scenarios.

In general, the data sets obtained in the four different scenarios exhibit very similar frequency content, with the exception of the data acquired when no power supply was connected. This data set displays higher intensity disturbances at frequencies in the 0.85 MHz - 1.10 MHz range than the remaining data sets in which the disturbances are have a somewhat lower relative amplitude. The lack of reverse bias in this condition could be a possible explanation for this effect, as it causes the APD to become more sensitive to disturbances.

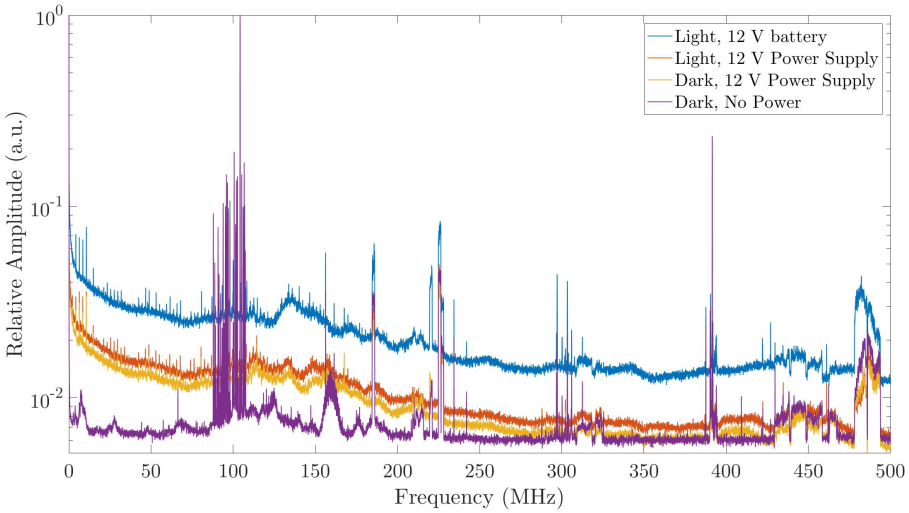

Figure 24: *Power spectra of background signal in LUMBO for varying conditions of the avalanche photodiode.*

The APD has a BW of 113 MHz, entailing that signals above this frequency most probably arise from EMI or disturbances in the power supply/battery as opposed to optical disturbances registered by the APD. Comparing the datasets from light and dark conditions with a 12 V power supply, there are no distinct disparities between the two, suggesting that any optical disturbances are limited.

Furthermore, it is evident that the relative amplitude of the low-frequency spectral content increases with the presence of a power supply or battery, implying that broadband disturbances are being introduced in both cases. Powering the APD with the battery seems to cause a spectrum-wide shift in relative amplitude, meaning that the relative height of the peak at 391.6 MHz is smaller in comparison to the remaining spectral content. The standard deviation of the spectral content from the APD powered by the battery is plotted alongside the power spectrum in Figure 25.

Figure 25 shows that the standard deviation for the peak at 391.6 MHz is lower than the average standard deviation, implying that the source of the disturbance is stable in time. As such, it is possible that the spectrum-wide shift in relative amplitude seen when using the battery is due to voltage noise [53].

It is reasonable to deduct that the majority of peaks shown in Figure 24 are the result of EMI arising from the interaction of exterior signals in the background with the electronics of the system. The peaks between 0.85 MHz - 1.10 MHz, for example, coincide very well with the frequencies at which local radio stations broadcast [54].

To assess the effects of sampling at lower sample rates in order to accommodate efficient data collection, the 1.25 GHz background time series data collected in light conditions and with a connected 12 V power supply was sampled at different rates, shifting the associated Nyquist frequency, N_f, to lower frequencies. The power spectra were obtained by performing a discrete Fourier transform on the data and are presented in Figure 26.

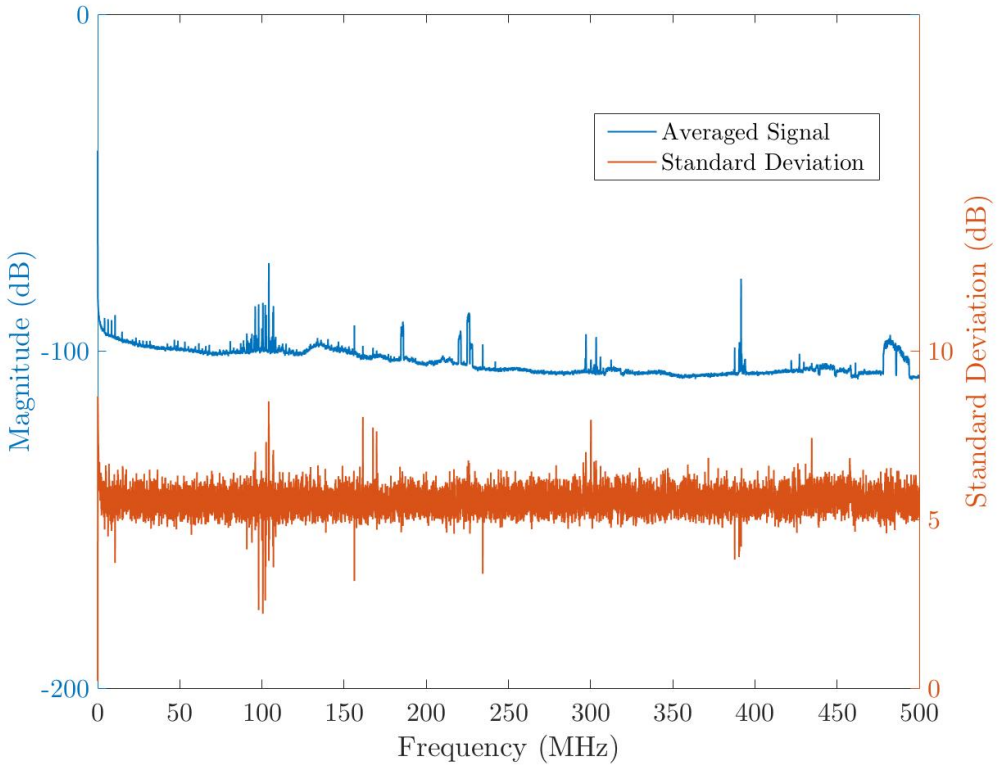

Figure 25: *Power spectrum of background signal in LUMBO as measured with the avalanche photodiode reverse biased with a 12 V battery and exposed to daylight, alongside the standard deviation associated with the frequency content. Low standard deviations indicate signals that are consistent in time whereas high standard deviations suggest a fluctuating signal.*

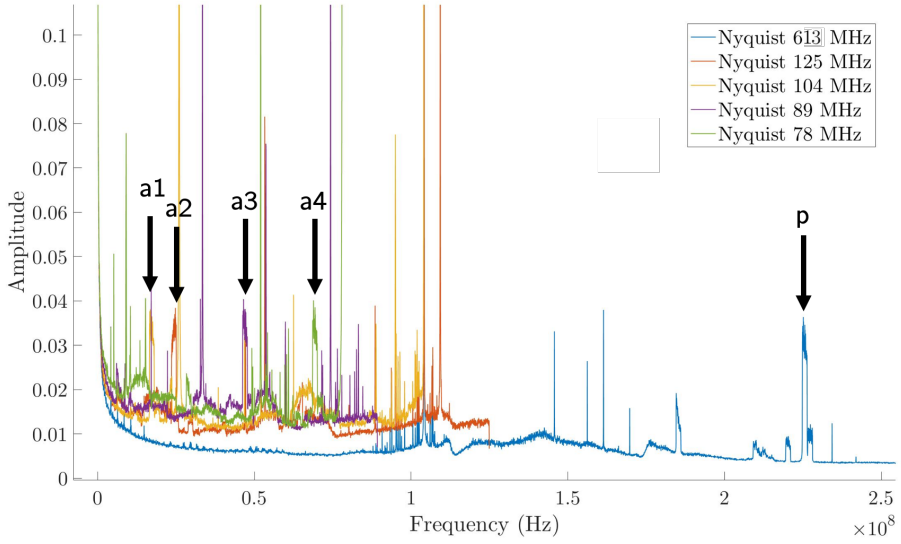

Figure 26: *Fourier transforms of the background signal obtained when sampling the APD in light conditions and reverse biased by a 12 V power supply at different sample rates and thus different associated Nyquist frequencies. Peak p at 225 Mhz is folded in the Nyquist frequencies of the other datasets to positions a1, a2, a3 and a4.*

The spectra arising from time series sampled at decreased rates (N_f = 125 MHz, 104 MHz, 89 Mhz, 78 MHz) display higher-amplitude baselines when compared to the spectrum at $N_f = 613$ MHz. Furthermore, in contrast to the original dataset at $N_f = 613$ MHz, the spectra with lower Nyquist frequencies are significantly noisier at the low-frequency end of the spectrum, exhibiting peaks not present in the original spectrum. Both of these effects arise from aliasing in the Nyquist frequencies. Several peaks seem to be aliased in the Nyquist frequencies, as explained in Section 6. For example, the structures labelled $a1, a2, a3$ and $a4$ in Figure 26 are similar in shape and relative amplitude to the structure p. In order to identify aliased peaks in the 125 MHz, 104 MHz, 89 MHz and 78 MHz spectra, the positions, f_p, of prominent peaks in the 613 MHz spectrum were identified and mirrored in the respective Nyquist frequencies to give the aliased positions. A selection of some of the prominent peaks, and their FWHM positions in the different datsets, are presented in Table 3.

Depending on the sampling frequency with which measurements are taken, the peaks listed in Table 3 or their aliased equivalents should be filtered from the data.

Table 3: *Identified background disturbances in LUMBO and the associated frequencies at which they appear when sampling at rates twice the Nyquist frequencies, N_f listed.*

Peak	**Position (MHz)** $N_f =$ **613 MHz**	**Aliased Position (MHz)**			
		$N_f =$ **125 MHz**	$N_f =$ **104 MHz**	$N_f =$ **89 MHz**	$N_f =$ **78 MHz**
1	487	13	70	49	18
2	391	109	26	34	78
3	303	53	95	54	10
4	225	25	17	46	69
5	185	65	23	6	29
6	161	89	47	18	5
7	104	104	104	75	52
8	102	102	102	77	54
9	101	101	101	78	55
10	95	95	95	84	61

7.2.3 Time-of-Flight Measurements

Figure 27 is a representative example of the signal obtained in one of the APD channels when terminating the Er:FL beam at the chemistry building. Data was collected by the oscilloscope in rapid block mode, with 1000 sets of data containing 10 waveforms for the four channels, each consisting of 1000 samples and sampled at an effective sample rate of 125 MHz.

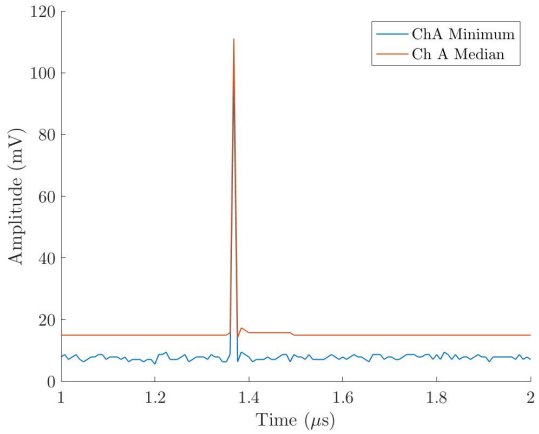

Figure 27: *The median and minimum signal in a single channel obtained from the wall of the chemistry building at which the Er:FL was terminated across* 10^7 *laser shots. The total TOF of the signal spanning 1.368* µs *corresponds to a detector-termination distance of 204.5 m.*

In the case of Figure 27, sampling took place at 1.25 GS/s in each channel and was downsampled by a factor 10 which led to a spatial resolution of 2.4 m. The dynamic range of the oscilloscope was set to ± 500 mV and the vertical resolution was 1.24 mV. There is a dark current in the channel around 18 mV and the peak at 1.368 µs represents the TOF of the laser pulse, translating into a detector-termination distance of 204.5 m. The FWHM of the termination peak is approximately 8 ns wide, or 125 MHz wide in the frequency domain. This is in agreement with the effective sample frequency after downsampling ($\frac{1.25\text{ GHz}}{10} = 125$ MHz).

Figure 28(a) displays the signal strength distribution in each channel at the time at which the termination echo registers on the APD, from which the dark current in the channels has been subtracted. Figure 28(b) conveys the noise distributions in the signal obtained prior to the arrival of the termination echo.

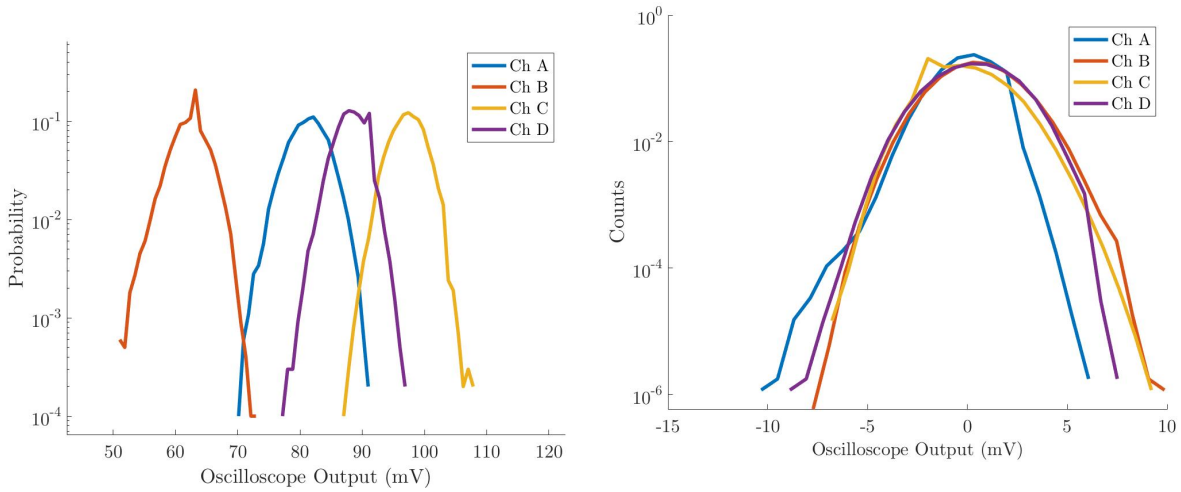

(a)

Figure 28: *Distributions of the measured signal intensity across the four channels for (a) the time bin in which the termination signal arrives and (b) the pre-termination time bins. The dark current in each respective channel is subtracted from the relevant distributions. Termination was at the wall of the chemistry building.*

From Figure 28(a), it is evident that the termination echo is not evenly distributed across the quadrants. As seen in Figure 28(b), the noise in all the channels follows similar Gaussian-like distributions, with a FWHM of approximately 4 mV. This implies that the SNRs for the channels differs between channels, from having a value of 24 in channel D to having a value of 15 in Channel B. Assuming that the beam is entirely collimated at the termination, it would have an area of $A_b = \pi \cdot (\frac{52}{2})^2\ \text{mm}^2 = 2124\ \text{mm}^2$. Taking the area of an airborne object, A_o, to be in the region of $A_o = \pi \cdot (\frac{5}{2})^2\ \text{mm}^2 = 20\ \text{mm}^2$, the backscattered signal from the object could be estimated to be a factor of $\frac{A_b}{A_o}$ smaller than that from the termination – in this example, therefore, the object signal would be a factor of 106 times smaller. The backscattered signal from the object would thus be indistinguishable from the noise. Referring back to Figure 14, it is possible that the reflectance of an insect, for example, would be higher than that of the red brick of the chemistry building, increasing the intensity of the backscattered light from the insect in relation to that from the termination. Reflections from insects at ranges shorter than the termination would also increase the intensity of the backscattered signal due to the inverse-square relationship between intensity and range, less atmospheric attenuation of the laser beam and an inherent variation in beam intensity with range as a result of beam divergence. Hence, detecting insects at short ranges could potentially be possible with the existing setup, but the arrangement is not currently able to reliably monitor insects of varying sizes at large distances.

The time at which the termination signal arrived at the APD was stable both in time and across the channels. During one test, however, the termination signal seemed to be consistently spread out across two time bins. By plotting the signal strength distribution similarly to in Figure 28(a), a representation of the termination image on the APD could be generated, as seen in Figure 29.

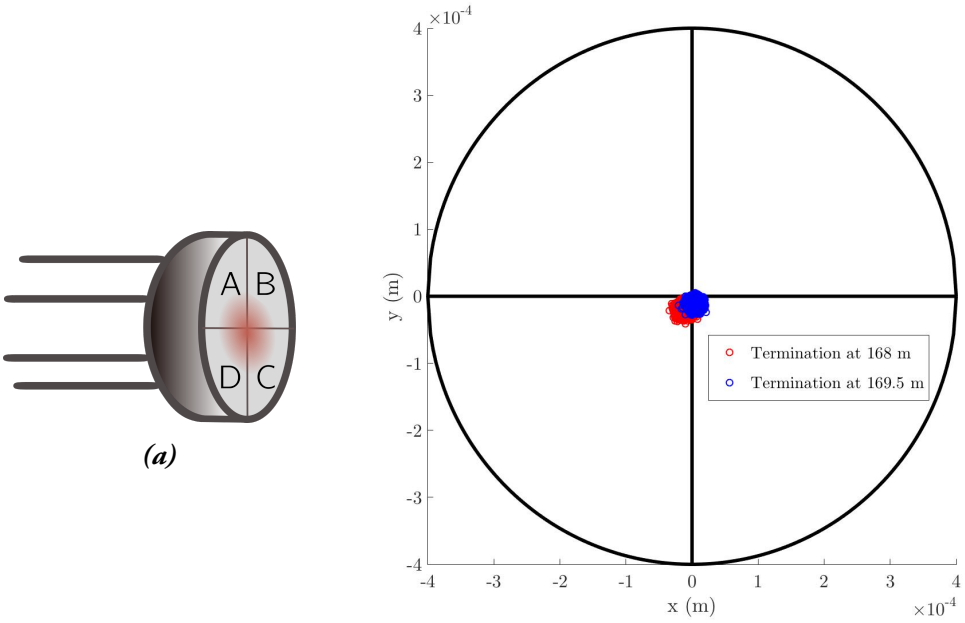

Figure 29: *a) Example of signal placement on APD active area and b) spatial distribution of termination signal, arriving between two time (and range) bins. The differing distributions are indicative of the APD FOV at the ranges in question.*

Figure 28(b) is an example of a case in which the laser is directed towards the termination at an angle, projecting the laser spot over a finite distance parallel to the emission direction. This causes variations in TOF from different regions within the projection and the signal is traced back to two different range bins. By mapping the spatial distribution of the backscattered signal from different ranges, the FOV of the different quadrants can be deducted and later used to extract, for example, the flight headings of an insect.

7.2.4 SNR Improvement

As previously mentioned, alternative impedances were applied to Channel A in an attempt to increase the SNR of the backscattered light from the wall of the Chemistry building. Figure 30 shows the results of these experiments, conveying the median signal acquired.

During the experiments performed to obtain the results shown in Figure 30, alignment was problematic and no strong signal could be obtained, as indicated by the small termination signal obtained at the standard impedance of 50 Ω in contrast to the signal shown in Figure 27. Although the amplitude increases, the FWHM of the termination peak around 1.2 µs experiences a significant increase with increasing impedance, to the extent that the spatial resolution of the system is severely compromised and the application of alternative impedances via a T-connector is not an appropriate method of amplifying the obtained APD signal. Unfortunately, the TIA built to bypass this problem experienced strong interference effects due to its design, causing it to heat up and introduce

heavy sinusoidal disturbances into the oscilloscope readings.

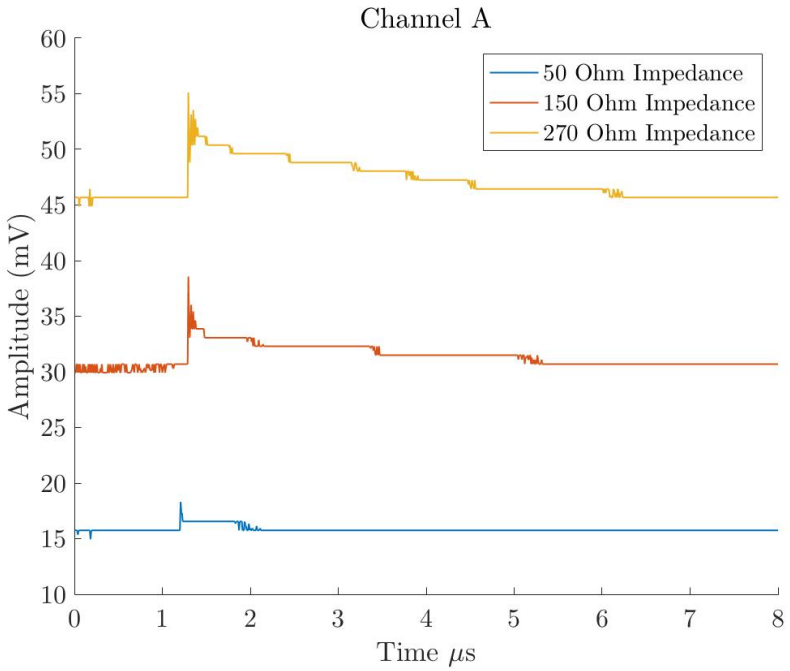

Figure 30: *Median signal obtained from TOF measurements on the wall of chemistry building for different impedances applied to Channel A.*

8 Scheimpflug Lidar

8.1 Experimental Setup and Methods

The Scheimpflug lidar set up is situated at Lund University, marked by the leftmost red circle in Figure 31. The design of the system is shown in Figure 32.

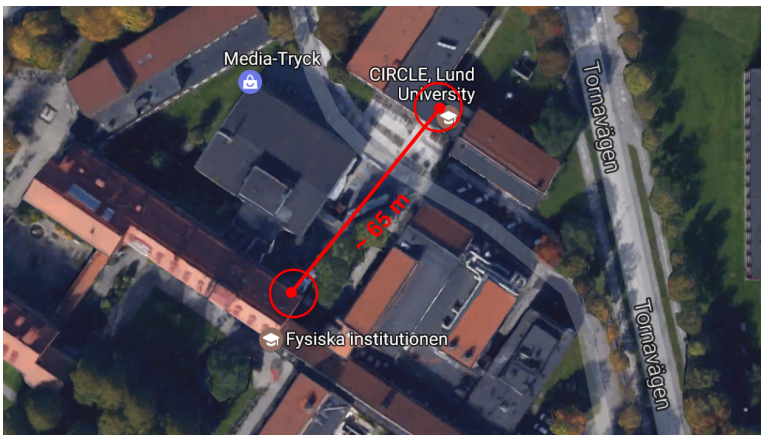

Figure 31: *Aerial view of the building from which Scheimpflug measurements were performed (marked by leftmost circle) and the wooden tunnel through which the lasers were aimed and in which particle experiments were performed (on right).*

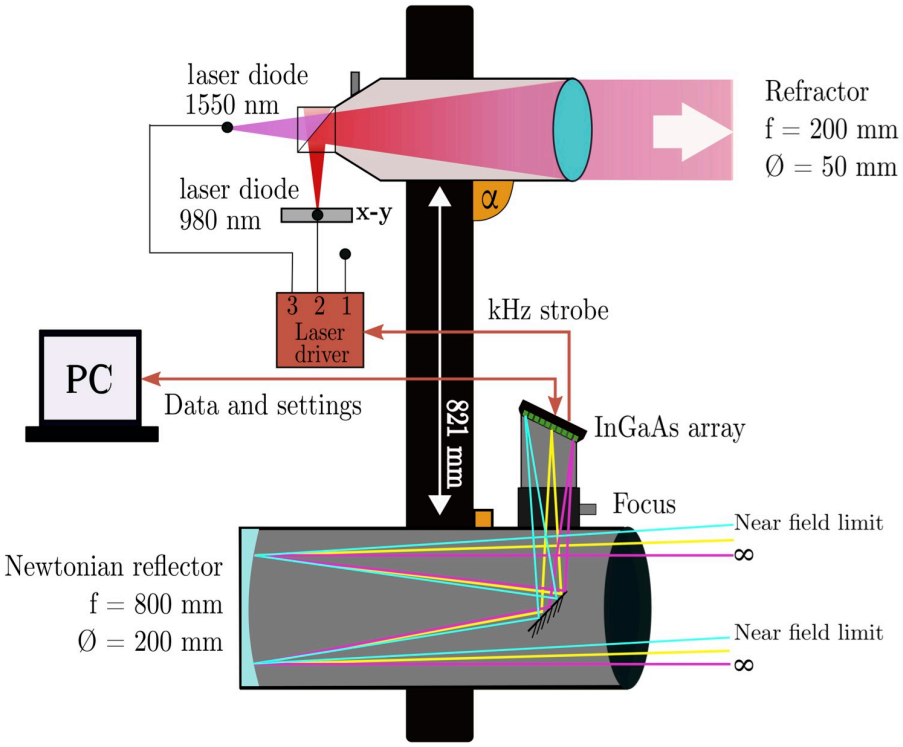

Figure 32: *Schematic showing the experimental setup of the Scheimpflug lidar equipment.*

A laser driver was configured to switch between three time slots: no laser, a 980 nm laser and a 1550 nm laser in the SWIR region. The total laser peak power was measured to be 4.2 W and 2.5 W respectively. With the use of a dichroic beamsplitter, the two laser beams were directed into a refractor by which they were expanded and emitted. Backscattered light was captured by a Newtonian reflector telescope. The reflector focussed the light onto the InGaAs 2048 pixel array, with pixel size 12 µm × 50 µm. The array was tilted at 45 ° with respect to the optical axis of the reflector, and transferred the signal to a PC. Not shown in Figure 32 is the Ximea camera used to image the 980 nm beam for alignment purposes. LabVIEW software was was used to control how fast switching between time slots took place, to adjust the number of time slots (lines) in a single frame and to obtain an overview of the signal during measurements. The ranging information was obtained as described in Section 1.2 and the near limit of the system was at 35 m. Due to a mismatch between available filters and the wavelengths of the lasers, the system was confined to night-time operation.

8.2 Alignment

The system was operated indoors through an open window and was pointed towards a hollow wooden tunnel on the roof of the CIRCLE building at Lund University, situated 65 m from the Scheimpflug setup. The laser beam was terminated on the Elite Hotel Ideon building, located approximately 980 m away.

Superposition of the two beams was obtained by directing the lasers onto the brick wall of the nearby CIRCLE building at Lund University, marked in Figure 31. The 980 nm beam was monitored by

the Ximea camera and scanned with the $x - y$ mount until both beams gave rise to a signal in the same range pixels on the InGaAs array. Once overlapped, the beams were pointed towards the black box on top of the Elite Hotel Ideon building. The focus on the refractor was adjusted to focus the laser beam on the termination, and the InGaAs array was rotated around the axis of the cylindrical extension tube in which it was fastened until the termination signal appeared around pixels 1800 to 2000 of the array. The presence of an atmospheric signal decaying with increasing range due to attenuation confirmed that focus along the whole laser beam had been attained and that the Scheimpflug condition (see Figure 1) had been fulfilled.

8.3 Dual Band Classification of Aerosols

In order to investigate the capabilities of dual band Scheimpflug lidar in the identification and classification of atmospheric aerosols, different types of aerosol were released in the wooden tunnel on the roof of the CIRCLE building during night-time and winter conditions. The aerosols included four types of soot, cement powder, ash and $NaHCO_3$, released with the aid of an inverted vacuum, water vapour released through exhalation and smoke released through the burning of a cardboard by the probe volume. The three time slots (1550 nm illumination, 980 nm illumination and "dark") were alternated between at a line rate of 500 Hz.

Signals above a threshold consisting of the static atmopsheric signal plus twice the noise were registered as es.

8.4 Dual Band Measurements of Insects

Scheimpflug measurements were performed in the month of July to acquire insect signals. As before, three time slots corresponding to 1550 nm, 980 nm and "dark" were implemented. The exposure time for each was 166 μs, giving an effective sample rate of 2 kHz for each respective channel (a line rate of 6 kHz).

8.5 Results and Discussion

8.5.1 Dual Band Classification of Aerosols

Figure 33 depicts an example of the spatiotemporal evolution of a particle plume imaged with the dual band Scheimpflug setup, in this case a sample of $NaHCO_3$. It conveys the diffusion of the $NaHCO_3$ plume along the laser beam with time. Initially, the plume spreads more towards shorter ranges. That is to say, the plume travels towards the Scheimpflug setup and the it can be concluded that the wind direction contains a component directed towards the equipment. Occasionally, emission plumes from vehicles travelling on the road behind the CIRCLE building were visible in the data.

The backscatter from particle plumes such as the one shown in Figure 33 was analysed first by subtracting the contribution in the dark time slot from the 1550 nm and 980 nm measurements to eradicate background, and then by comparing the backscattered light in 1550 nm to that in 980 nm in two consecutive time slots (laser lines). Doing so generated distinct distributions for different kinds of particles, with the midline contour for three of these distributions conveyed in Figure 34.

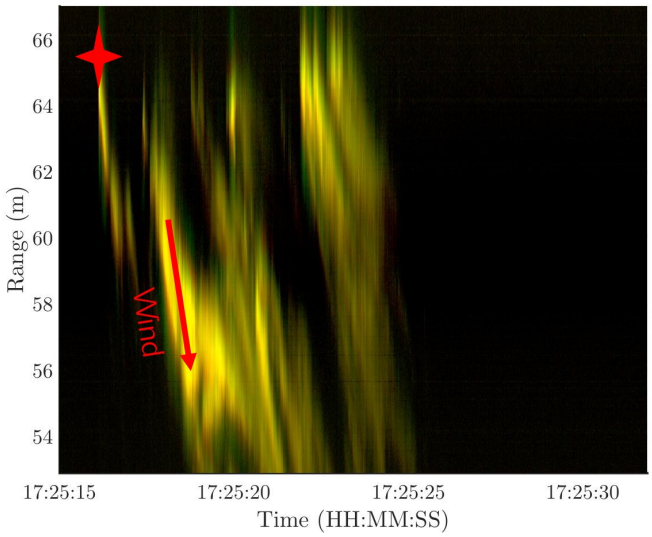

Figure 33: *Composite false colour time-range map, depicting the evolution of a sample of $NaHCO_3$ with time, from its release point marked by the red star. The dispersal of the sample towards shorter ranges suggests a wind velocity with a direction component pointed towards the setup.*

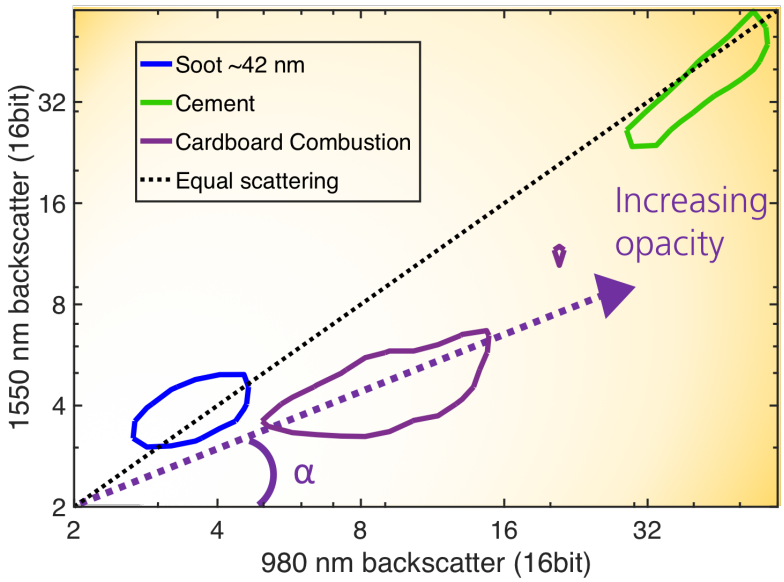

Figure 34: *Curves showing the midline contour of the 2D distribution of the scattering intensities in the many time-range pixels from each particle plume released. The distance from the origin indicates particle concentration while the spectral slope is indicative of particle species.*

The distribution contours of the three aerosols depicted in Figure 34, although all elliptical in shape, convey distinct differences with respect to radial distance from the origin and angular position. Aerosol concentration, not controlled in this experiment, should affect the extinction coefficient and subsequently the intensity of the scattered light, shifting the midline contour of the particle scatter-

ing distribution further from the origin the more concentrated a sample is. With this reasoning, it is highly likely that the cement sample in Figure 34 was of a higher concentration than the particulate content in the smoke originating from the cardboard combustion. Aerosol concentration, however, should not affect the scattering spectral slope. The angle α describing the position of a distribution is therefore indicative of its scattering coefficient. Referring back to Sections 2 and 3 and Figure 9, it was explained that scattering coefficient is a result of the unique properties of a medium in addition to the wavelength of the incident radiation and the particle diameter. As such, the spectral slope varies between aerosols and this method can be used to distinguish between different samples. The scattering distributions with respect to spectral slope are presented in Figure 35.

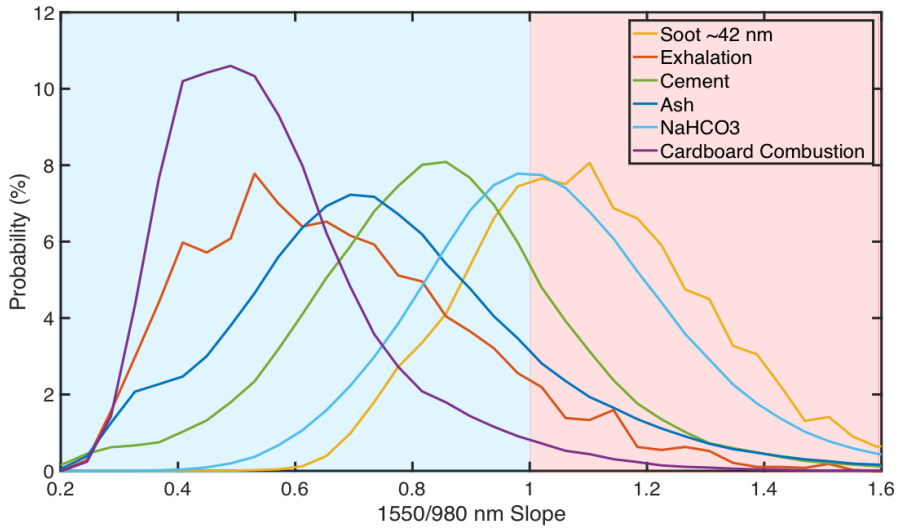

Figure 35: *Histograms of the spectral slope pertaining to the different particle specimens released in the Scheimpflug particle release experiments.*

From Figure 35, it appears that preferential scattering towards 1550 nm occurs only for the soot sample, while the remaining aerosols scatter towards 980 nm. This is in agreement with the simulation on Mie scattering from water particles, shown in Figure 9. The steepest spectral slopes are seen in the ”exhalation” and ”cardboard combustion” (smoke) samples. H_2O, present in water vapour, and CO_2, produced during combustion, both have absorption lines in the 1550 nm region [55] [56]. The laser used, however, was an uncontrolled temperature multimode laser diode, presumably with a large spectral bandwidth. It is possible that the water vapour formed very small solid water particles due to the ambient temperature of $-12°C$, scattering more at shorter wavelengths than at longer wavelengths. Preferential scattering of the 980 nm laser light, therefore, is reasonable and to be expected. The spectral slope distributions of the various aerosols act as a signature, or fingerprint, characterising each particle type.

If a particle sample scatters more towards 980 nm, the spectral slope distribution is shifted towards the blue side of Figure 35, whereas a preferential scattering in 1550 nm leads to a distribution shift towards the red side. The spectral slope of the soot sample (42 nm) is the only sample in Figure 35 to show stronger scattering in 1550 nm (as measured by the position of the median of the distribution); it is represented as a Box and Whisker plot together with the three remaining soot

samples in Figure 36.

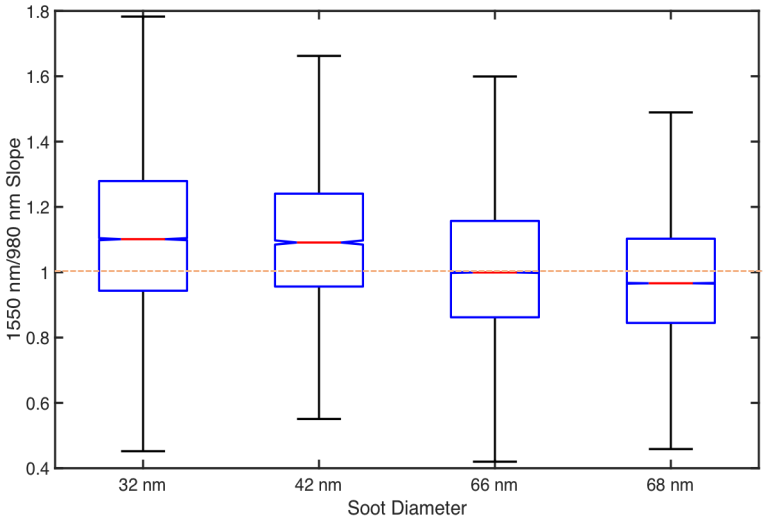

Figure 36: *Box and whisker plots of the scattering ratios (spectral slopes) from measurements on four soot samples with varying primary particle diameters. The red line represents the median of the data set, the upper and lower edges of the box represent the interquartile range (IQR). 99.3% of the data is contained within the whiskers.*

Judging by Figure 36, it seems that the larger the primary particle size of the soot, the more scattering occurs in 980 nm relative to 1550 nm. However, as discussed in Section 2, Rayleigh scattering occurs at wavelengths much larger than the particle diameter, as is the case with the four soot samples, and scales with λ^{-4}. From a physical point of view, it is thus not supported by scattering theory that scattering from the soot particles should be stronger in the 1550 nm regime. One possible reason for the controversial preferential scattering towards larger wavelengths could be that the primary particles form aggregates of various shapes and sizes. In particular, the soot samples with primary particle size 66 nm and 68 nm form large structures of approximately 500 nm in length [57]. At relatively large particle diameters (>10 μ m), the difference in backscattered intensity between 980 nm and 1550 nm is not as pronounced as for particles with smaller diameters (see Figure 9). The larger structures could potentially lead to the less wavelength-dependent Mie scattering instead of Rayleigh scattering, explaining the small difference in relative scattering in 980 nm and 1550 nm, as well as the small variation between the sample sets. It should not be forgotten that the Mie and Rayleigh theory mentioned make the assumption that the spherical particles in question are spherical; this is most certainly not the case for the soot particles. As such, the unexpected results could perhaps be attributed to the irregularity of the soot particles.

Although the medians of the datasets are statistically separated from each other, all of the soot distributions show large spread and further experiments are in any case required to confirm the presence of the aforementioned trend in the data.

8.5.2 Dual Band Measurements on Insects

Figures 37 and 38 portray the time series data and corresponding Fourier transform of a single insect event respectively, captured at wavelengths of 1550 nm and 980 nm.

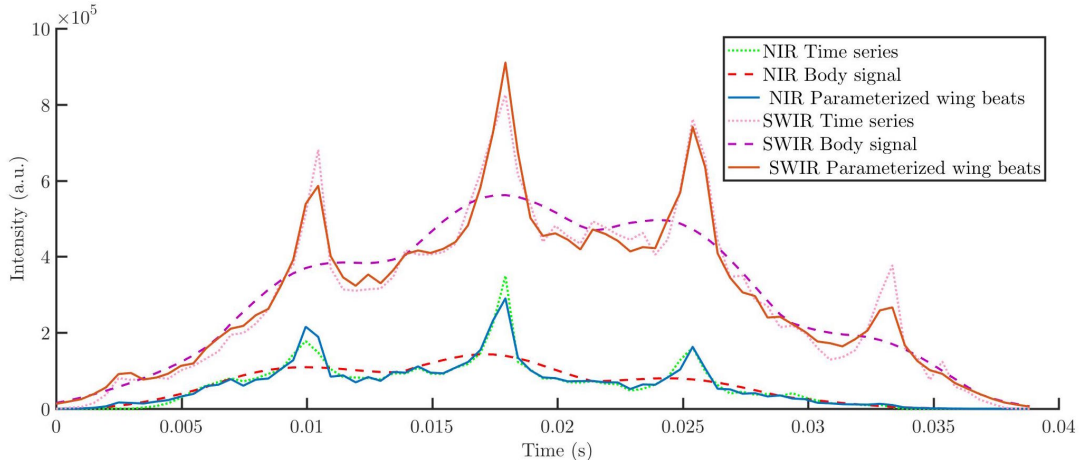

Figure 37: *Time series data of an insect signal measured at a SWIR wavelength of 1550 nm and a NIR wavelength of 980 nm, showing the body, wing-beat and combined contributions respectively. The separation into body and wing contributions is performed by a manual wing beat analysis script. Measurements performed at a sample frequency of 2 kHz (6 kHz line rate). The relative differences between the two wavelengths in transmittance through the long-pass filter have been corrected for.*

In both the SWIR and NIR regimes, the intensity of the signal (and the OCS) oscillates with time as described in Section 4.1. The SWIR signal reveals four distinct wing beats, while the NIR signal shows only three.

The SWIR signal in Figure 37 is significantly higher than that of the NIR signal. This is partially to be expected from the higher average laser power (see Table 1). Assuming that the spectral response of the InGaAs is equal at 980 nm and 1550 nm, as suggested by [58], a stronger signal in 1550 nm points toward a higher reflectance in 1550 nm. It is assumed that the spectral response of a bumblebee in the NIR-SWIR spectral domain is representative of the insect observed in Figure 37. Looking back at Figure 12, it is evident that the insect reflectance at 1550 nm is strongly dependent on the path length through water. In other words, the reflectance depends largely on the size and water content of the insect. It also depends on the presence of any fur which way shield the tissue. If the water content of all insects can be taken to be roughly identical, the relative intensity between the NIR and SWIR band can be used to determine the lengths of the respective scattering paths in the insect. The lengths of the scattering paths are, in turn, a measure of the scattering coefficient and can be used to identify the species.

The Fourier transforms of the time-series signals are presented in Figure 38. Thse both indicate a WBF of 127 Hz, with associated higher harmonics. The SWIR band resolved three clear higher harmonics and the Fourier transform of the NIR band data gave four harmonics, despite the lower intensity. With a Nyquist frequency of 1 kHz, up to six harmonics should theoretically be visible at the given WBF.

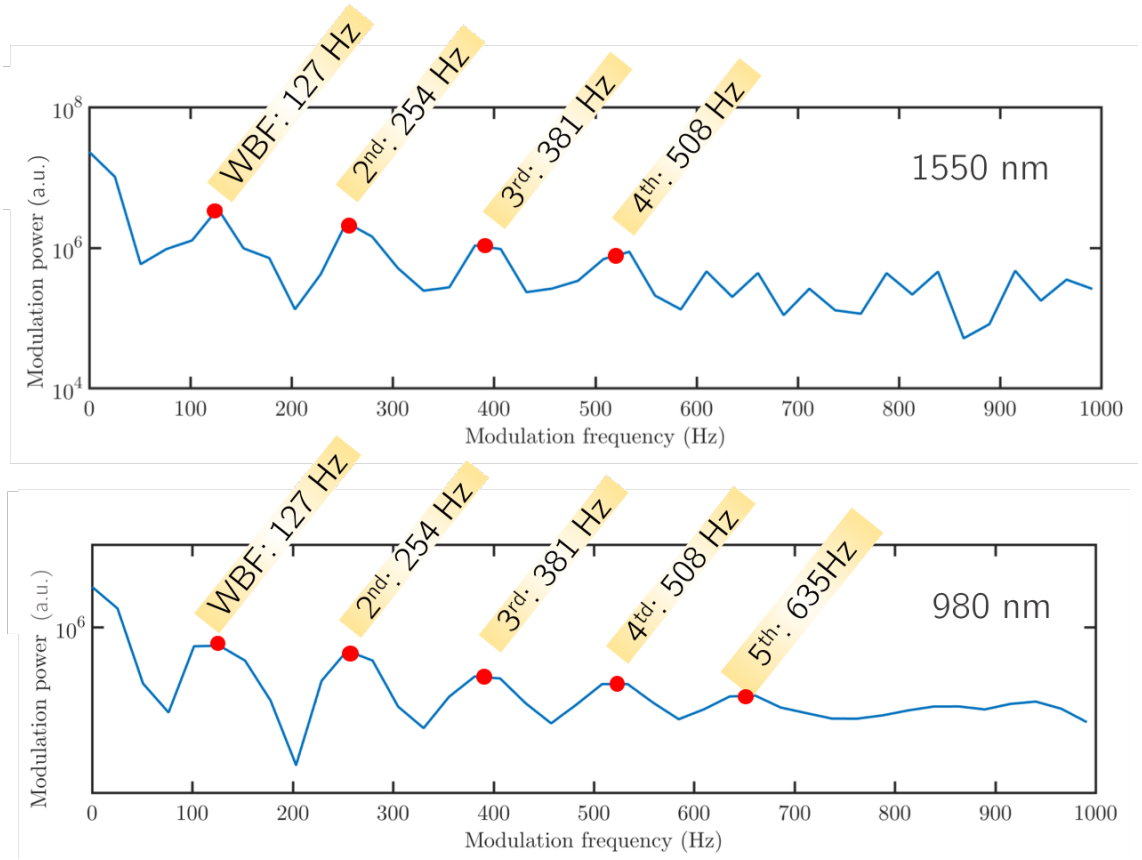

Figure 38: *Fourier Transforms of the time series data shown in Figure 37 depicting the WBF peak and three discernable harmonics.*

Part IV

Conclusion and Outlook

Efforts have been made to implement two elastic lidar techniques for short wave infrared measurements on atmospheric aerosols and insects.

To bring the TOF system into a state in which measurements could be performed, an optical trigger was constructed and software was developed to tailor the data acquisition to a form suitable for entomological lidar. The software ran an order of magnitude slower than the quoted speeds, implying a delay between acquired data sets that would be significant enough to affect the suitability of the acquistion method in the context of entomological lidar campaigns. In order to reduce the time taken for the software to run, the raw analogue data (16 bit integer) could be stored as opposed to the double-precision 64 bit floating point numbers. Although this would not bring the software up to quoted speeds, it would offer some improvement.

It was deduced that the sources of the background signal present in the equipment at LUMBO were primarily as a result of electromagnetic interference between external signals and the system

electronics. Optical and mains disturbances were not equally significant. A list of significant peaks to filter from the data was identified and presented for future use. The TOF registered for the round-trip distance between LUMBO and the chemistry building corresponded well with a distance of approximately 200 m. The signal obtained from the wall of the chemistry building, however, had SNRs between 15 and 24, meaning that any potential insect signals would not be discriminated from the noise. Although the signals obtained were too low to identify any aero-fauna, the potential of using the APD to map the FOV at different distances from the detector was exemplified when the termination signal was spread between two different range bins. Unfortunately, attempts to increase the amplitude and SNR of the termination signal by application of alternative impedances and the manufacture of a transimpedance amplifier were unsuccessful. The alternative impedances resulted in very poor spatial resolution and the TIA was subject to strong interference effects that rendered it inoperative.

Should the data acquisition software be redeveloped in order to avoid the source of the lag, if possible, the APD signal would be able to be sampled at a high enough frequency and for sufficiently long durations to register insect events and their higher harmonics. A redesign of the TIA is also crucial to the future performance of the TOF system – with a higher APD BW, the only limiting factor on spatial resolution would be the pulse width at 6 ns. Should these changes and the purchase of suitable filters be made to decrease the ambient signal, the TOF system shows great potential as a technique for the detailed study of aero-fauna. Given the system specifications mentioned in Section 1.3, the LUMBO system could potentially offer a significant improvement in terms of sensitivity and measurement range compared to previous measurements. Additionally, the use of a quadrant APD opens up for the possibility to register movement of insects within the beam and perform experiments on e.g. insect flight direction during different conditions.

Dual band measurements on both aerosols/particle plumes and insects were performed with the Scheimpflug setup. The proof-of-concept measurements on particle plumes demonstrated the spatio-temporal abilities of the technique by showing how the plume evolved from its release point. Given that even emission plumes from vehicles were occasionally registered in the data, the technique shows promise in the detection and localisation of pollution sources. Moreover, the comparison of the plume signals in terms of spectral slope and opacity showed that the Scheimpflug lidar method is capable of distinguishing different particles/aerosols from each other. Dual band measurements performed on insects demonstrate the ability of the Scheimpflug setup to resolve not only the WBFs of insects, but also several higher harmonics, in two wavelengths at the same time. Similarly to the particle measurements, the dual band measurements could potentially be analysed in order to serve as a basis for species identification.

Further experiments on particles with the Scheimpflug setup could involve a more controlled release of particles and different samples. More information regarding the particle samples, obtainable through microscopy, would have been desirable. Moreover, it would be interesting to map bulk atmospheric gases at the high spatiotemporal resolution provided by the Scheimpflug infrastructure; this could be done by modifying the laser wavelengths to target the absorption lines of the gases in question.

In conclusion, many atmospheric gases and molecules present in living organisms show structure in the SWIR regime. Combined with the fact that SWIR wavelengths can be used at high power densities owing to the fact that certain wavelengths are relatively eye safe, the lidar methods discussed

in this thesis show great potential as methods of monitoring aeorosols and aero-fauna with improved sensitivity and resolution.

9 Acknowledgements

There are many people to whom I owe my thanks for supporting me during my thesis work, and without whom it would not have been possible.

First and foremost, thank you to my supervisor, Mikkel for teaching, inspiring and helping me.

Thank you, Samuel, for spending countless hours in the lab with me, for all the helpful discussions and for the great company inside and outside of the university environment.

Thank you, Jim, for all of your support in the lab and Elin for all the discussions and poster design advice.

Thank you, Joakim, for all of your advice and guidance during the weekly meetings.

Igor deserves so many thanks for putting up with all of the non-functioning laptops and soldering requests that came his way.

Thank you Jeremias and Christian, for all of the lovely office times.

Thanks to the rest of the employees and students at Combustion Physics who made every lunch a delight and these two semesters unforgettable.

Appendix A: Photodiode Construction

The photodiode constructed to act as an optical trigger in the LUMBO TOF system was constructed according to the circuit diagram shown in Figure 39.

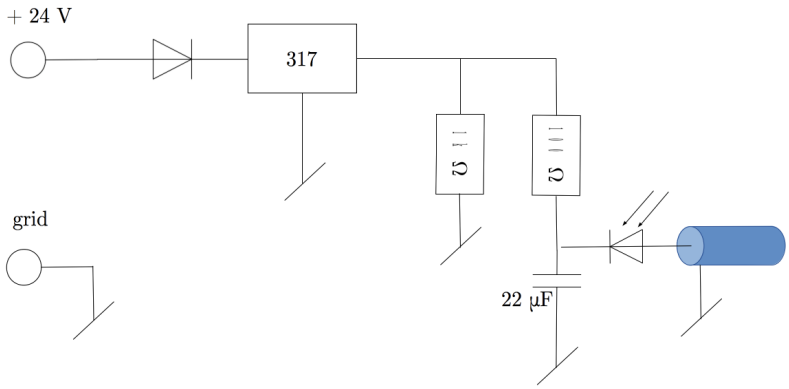

Figure 39: *Circuit diagram of photodiode constructed to act as optical trigger in LUMBO TOF system.*

Appendix B: Avalanche Photodiode BODE Plots

The following BODE plots depicting the simulated frequency response of the InGaAs APD in the LUMBO TOF system are sourced from email communication with the manufacturer, Princeton Lightwave.

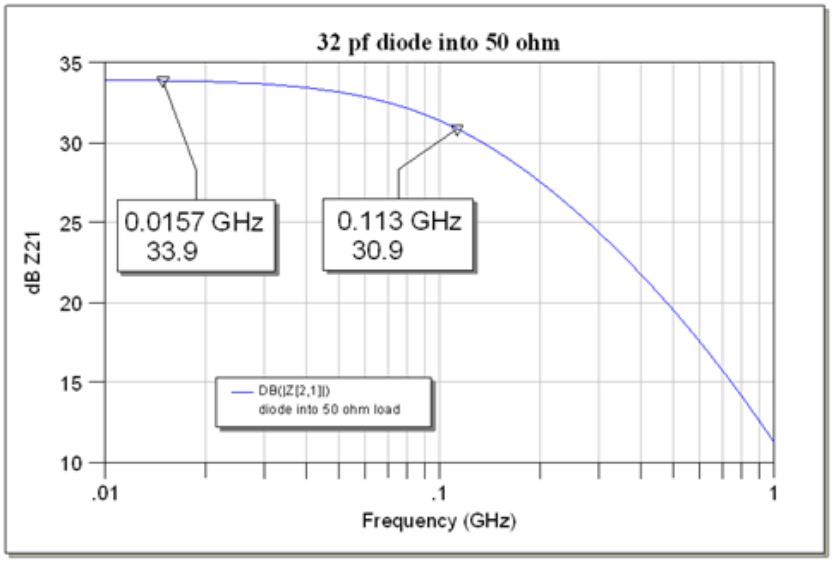

Figure 40: *BODE Plot of APD Performance. BW = 113 MHz.*

The manufacturer proposed the use of a transimpedance amplifier to increase the bandwidth of the APD.

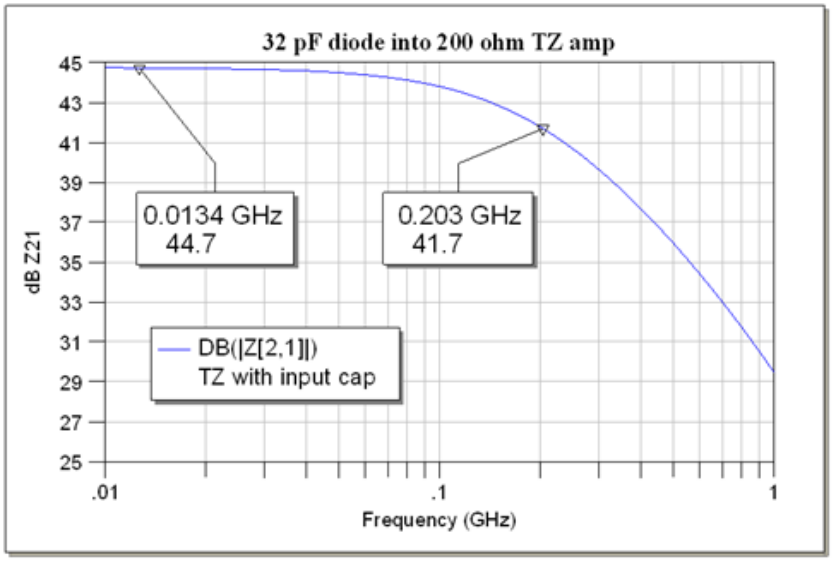

Figure 41: *BODE Plot of simulated APD Performance with transimpedance amplifier. BW = 203 MHz*

Appendix C: Transimpedance Amplifier Design

Princeton Lightwave proposed that a TIA be incorporated with the APD according to the circuit diagram shown in Figure 42 to increase the SNR.

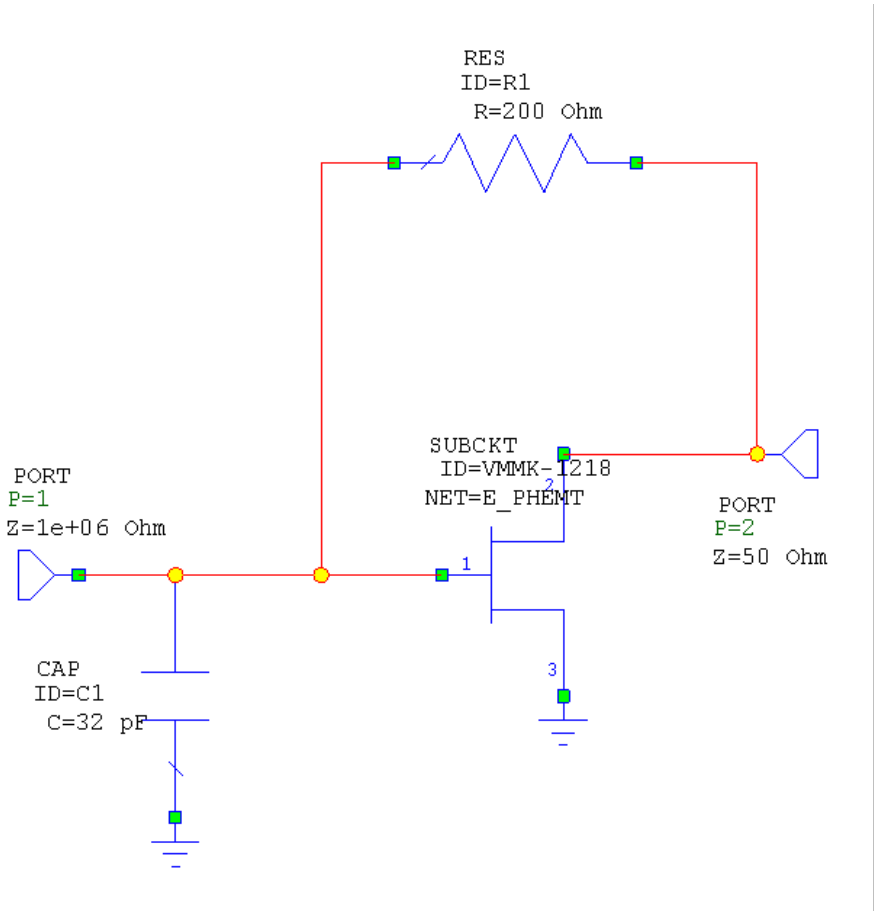

Figure 42: *Proposed circuit design, incorporating a TIA to increase APD BW. Diagram sourced from mail communication with the manufacturer, Princeton Lightwave.*

The TIA used in the simulation from Princeton Lightwave was of model VMMK-1218 from Avago. The circuit consists of appropriate biasing circuits, and a 200 ohm feedback resistor (0402) from the drain to the gate. The 32 pF capacitor at the input represents the diode junction capacitance and is not a separate component.

An image of the circuit board soldered for the purposes of this thesis, and including TIAs on each APD channel, is shown in Figure 43.

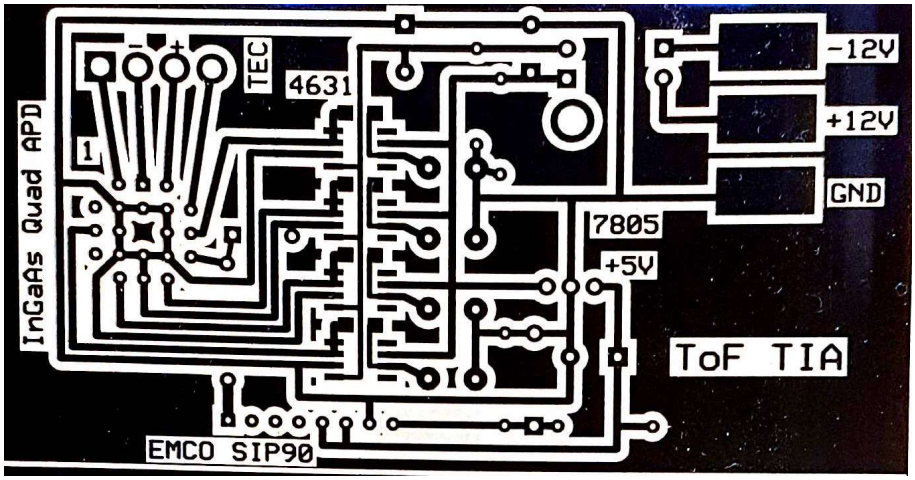

Figure 43: *Image of the unsuccessful circuit design with four TIAs on each APD channel*

References

[1] G JONES and E TEELING. "The evolution of echolocation in bats". In: *Trends in Ecology & Evolution* 21.3 (2006), pp. 149–156. DOI: 10.1016/j.tree.2006.01.001.

[2] E.H. Synge. "XCI. A method of investigating the higher atmosphere". In: *The London, Edinburgh, and Dublin Philosophical Magazine and Journal of Science* 9.60 (1930), pp. 1014–1020.

[3] David E. Smith et al. "Mars Orbiter Laser Altimeter: Experiment summary after the first year of global mapping of Mars". In: *Journal of Geophysical Research: Planets* 106.E10 (2001), pp. 23689–23722. ISSN: 2156-2202.

[4] Constantin Ilas. "Electronic sensing technologies for autonomous ground vehicles: A review". In: *2013 - 8th International Symposium on Advanced Topics in Electrical Engineering, ATEE 2013*. 2013. ISBN: 9781467359801. DOI: 10.1109/ATEE.2013.6563528.

[5] Edward J. Hyer and Boon Ning Chew. "Aerosol transport model evaluation of an extreme smoke episode in Southeast Asia". In: *Atmospheric Environment* 44.11 (2010), pp. 1422–1427.

[6] J. Lelieveld et al. "The contribution of outdoor air pollution sources to premature mortality on a global scale." In: *Nature* 525.7569 (2015), pp. 367–371.

[7] Claus Weitkamp. *Lidar. [electronic resource] : Range-Resolved Optical Remote Sensing of the Atmosphere*. Springer Series in Optical Sciences: 102. New York, NY : Springer Science+Business Media Inc., 2005., 2005. ISBN: 9780387251011.

[8] Mikkel Brydegaard, Alem Gebru and Sune Svanberg. "Super Resolution Laser Radar with Blinking Atmospheric Particles—-Application to Interacting Flying Insects". In: *Progress In Electromagnetics Research* 147.147 (2014), pp. 141–151. ISSN: 1559-8985.

[9] Samuel Jansson et al. "Exploitation of Multi-Band Lidar for the Classification of Free-Flying Migratory Birds: A Pilot Study Over Athens, Greece". In: *EPJ Web of Conferences* 119.January (2016), p. 27002. DOI: 10.1051/epjconf/201611927002.

[10] D. R. Reynolds and J. R. Riley. "Remote-sensing, telemetric and computer-based technologies for investigating insect movement: A survey of existing and potential techniques". In: *Computers and Electronics in Agriculture* 35.2-3 (2002), pp. 271–307.

[11] Drake V.A. and Reynolds D.R. *Radar entomology: Observing insect flight and migration*. 2012, pp. 1–489. arXiv: arXiv:1011.1669v3.

[12] J.R Riley and A.D Smith. "Design considerations for an harmonic radar to investigate the flight of insects at low altitude." In: *Computers and Electronics in Agriculture* 35 (2002), pp. 151–169.

[13] Otso Ovaskainen et al. "Tracking Butterfly Movements with Harmonic Radar Reveals an Effect of Population Age on Movement Distance." In: *Proceedings of the National Academy of Sciences of the United States of America* 49 (2008), p. 19090. ISSN: 00278424.

[14] V A Drake. "International Journal of Remote Estimation of unbiased insect densities and density profiles with vertically pointing entomological radars". In: *International Journal of Remote Sensing* 35.March 2015 (2015), pp. 37–41. ISSN: 13665901. DOI: 10.1080/01431161.2014.919682.

[15] Mikkel Brydegaard. "Towards quantitative optical cross sections in entomological laser radar - Potential of temporal and spherical parameterizations for identifying atmospheric fauna". In: *PLoS ONE* 10.8 (2015).

[16] A. Moore and R. H. Miller. "Automated identification of optically sensed aphid (Homoptera: Aphidae) wingbeat waveforms." In: *Annals of the Entomological Society of America* 95.1 (2002), pp. 1–8.

[17] Carsten Kirkeby, Maren Wellenreuther and Mikkel Brydegaard. "Observations of movement dynamics of flying insects using high resolution lidar". In: *Nature Publishing Group* Llc (2016), pp. 1–11. DOI: 10.1038/srep29083.

[18] Anna Runemark et al. "Rare events in remote dark-field spectroscopy: An ecological case study of insects". In: *IEEE Journal on Selected Topics in Quantum Electronics* 18.5 (2012), pp. 1573–1582.

[19] Peter G. Kevan. "Pollinators as bioindicators of the state of the environment: Species, activity and diversity". In: *Agriculture, Ecosystems and Environment* 74.1-3 (1999), pp. 373–393.

[20] Joseph Shaw et al. "Polarization lidar measurements of honey bees in flight for locating land mines." In: *Optics express* 13.15 (2005), pp. 5853–5863.

[21] Kevin S. Repasky et al. "Optical detection of honeybees by use of wing-beat modulation of scattered laser light for locating explosives and land mines". In: *Applied optics* 45.8 (2006), pp. 1839–1843.

[22] David S Hoffman et al. "Range-resolved optical detection of honeybees by use of wing-beat modulation of scattered light for locating land mines." In: *Applied optics* 46.15 (2007), pp. 3007–3012.

[23] Erik S Carlsten et al. "Field demonstration of a scanning lidar and detection algorithm for spatially mapping honeybees for biological detection of land mines." In: *Applied optics* 50 (2011), pp. 2112–2123. DOI: 10.1364/AO.50.002112.

[24] Theodor Scheimpflug. “Improved Method and apparatus for the Systematic Alteration or Distortion of Plane Pictures and Images by Means of Lenses and Mirrors for Photography and for other purposes”. In: February (1904), p. 52.

[25] Mikkel Brydegaard. “New mobile observatory for aero-fauna studies”. In: *SPIE Newsroom* November (2015), pp. 8–11.

[26] Jean-Claude Diels and Wolfgang Rudolph. “1 - Fundamentals”. In: *Ultrashort Laser Pulse Phenomena (Second Edition)*. Ed. by Jean-Claude Diels and Wolfgang Rudolph. Second Edition. Burlington: Academic Press, 2006, pp. 1–60. ISBN: 978-0-12-215493-5. DOI: https://doi.org/10.1016/B978-012215493-5/50002-1. URL: http://www.sciencedirect.com/science/article/pii/B9780122154935500021.

[27] Sune Svanberg. *Atomic and molecular spectroscopy : basic aspects and practical applications.* Advanced texts in physics. Berlin : Springer , cop. 2004, 2004. ISBN: 3540203826.

[28] Craig F Bohren and Donald R Huffman. *Absorption and scattering of light by small particles*. Vol. 98. 1983, p. 12. ISBN: 047105772X. DOI: 10.1038/ncomms1111.

[29] Eugene Hecht. *Optics 4th edition*. 2001. DOI: 10.1119/1.3274347.

[30] G M Hale and M R Querry. “Optical Constants of Water in the 200-nm to 200-microm Wavelength Region.” In: *Applied optics* 12.3 (1973), pp. 555–563. ISSN: 0003-6935. DOI: 10.1364/AO.12.000555.

[31] L. S. Rothman et al. “The HITRAN database: 1986 edition”. In: *Appl. Opt.* 26.19 (Oct. 1987), pp. 4058–4097.

[32] William C. Malm. *Visibility*. Ed. by William C. Malm. Elsevier, 2016, pp. 29–72.

[33] Christian Maetzler. *MATLAB Functions for Mie Scattering and Absorption*. June 2002.

[34] Mikkel Brydegaard et al. “Short-Wave Infrared Atmospheric Scheimpflug Lidar”. In: ().

[35] Albert Ansmann, Maren Riebesell and Claus Weitkamp. “Measurement of atmospheric aerosol extinction profiles with a Raman lidar”. In: *Opt. Lett.* 15.13 (July 1990), pp. 746–748. DOI: 10.1364/OL.15.000746.

[36] Liang Mei and Mikkel Brydegaard. “Continuous-wave differential absorption lidar”. In: *Laser and Photonics Reviews* 9.6 (2015), pp. 629–636.

[37] Simone Santoro et al. “Volcanic Plume CO2 Flux Measurements at Mount Etna by Mobile Differential Absorption Lidar”. In: *Geosciences* 7.1 (2017). ISSN: 2076-3263. DOI: 10.3390/geosciences7010009. URL: http://www.mdpi.com/2076-3263/7/1/9.

[38] Mei Liang, Guan Peng and Yang Yang. “Atmospheric aerosol measurements by employing a polarization Scheimpflug lidar system”. In: (To be published).

[39] Huige Di et al. “Vertical distribution of optical and microphysical properties of smog aerosols measured by multi-wavelength polarization lidar in Xian, China”. In: *Journal of Quantitative Spectroscopy and Radiative Transfer* 188 (2017). Advances in Atmospheric Light Scattering: Theory and Remote Sensing Techniques, pp. 28–38.

[40] Nianwen Cao et al. “Identification of aerosol species using polarization lidar.” In: *Optics Spectroscopy* 117.3 (2014), pp. 486–491. ISSN: 0030400X.

[41] Steven L Jacques. “Optical properties of biological tissues: a review.” In: *Physics in medicine and biology* 58.11 (2013), R37–61. ISSN: 1361-6560. DOI: 10.1088/0031-9155/58/11/R37.

[42] Eugene H. Studier and Steven H. Sevick. “Live mass, water content, nitrogen and mineral levels in some insects from south-central lower michigan”. In: *Comparative Biochemistry and Physiology – Part A: Physiology* 103.3 (1992), pp. 579–595. ISSN: 03009629. DOI: 10.1016/0300-9629(92)90293-Y.

[43] Elin Malmqvist and Mikkel Brydegaard. “Applications of khz-cw lidar in ecological entomology”. In: Llc (2016), pp. 4–7.

[44] Elin Malmqvist et al. “Effective parameterization of laser radar observations of atmospheric fauna”. In: *IEEE Journal on Selected Topics in Quantum Electronics* 22.3 (2016). DOI: 10.1109/JSTQE.2015.2506616.

[45] A. M. Baldridge et al. “The ASTER Spectral Library Version 2.0.” In: *Remote Sensing of Environment* 113 (2009), pp. 711–715.

[46] Simone Santoro et al. “Volcanic Plume CO2 Flux Measurements at Mount Etna by Mobile Differential Absorption Lidar”. In: *Geosciences* 7.1 (2017), p. 9.

[47] Wikimedia Commons. “Spectrum of Solar Radiation (Earth) based on American Society for Testing and Materials (ASTM) Terrestrial Reference Spectra data”. In: ().

[48] C E Shannon. “Communication_in_the_Presence_of_Noise”. In: *Proceedings of The IEEE* 3.2 (1998), pp. 1–11.

[49] P M Moretti. *Modern Vibrations Primer*. Mechanical engineering. Taylor & Francis, 1999, p. 183.

[50] Silicon Laboratories. *AN118 Improving ADC Resolution by Oversampling and Averaging*. URL: https://www.silabs.com/documents/public/application-notes/an118.pdf (visited on 17/07/2017).

[51] Pico Technology. “PicoScope 6000 ©Series Programmer’s Guide”. In: (2016).

[52] Mathworks. *Floating-Point Numbers*. May 2017. URL: https://se.mathworks.com/help/matlab/matlab_prog/floating-point-numbers.html.

[53] C.K. Boggs, A.D. Doak and F.L. Walls. “Measurement of voltage noise in chemical batteries”. In: *Proceedings of the 1995 IEEE International Frequency Control Symposium (49th Annual Symposium)* January 1995 (1995), pp. 367–373.

[54] Teracom. *Frekvenstabeller för radio*. May 2017. URL: https://www.teracom.se/privat/radio/frekvenstabeller-radio/.

[55] National Institute of Standards and Technology (NIST). “Coblentz no. 10116 for water”. In: (1969).

[56] National Institute of Standards and Technology (NIST). “Coblentz no. 8753 for carbon dioxide”. In: (1964).

[57] Nils Hernäng. “Experimental Investigations on Carbon Black Aerosols”. In: *Master Thesis at Lund University* April (2009).

[58] Hamamatsu. “Infrared Detectors”. In: *Selection Guide* (2017). URL: http://www.hamamatsu.com/resources/pdf/ssd/infrared_kird0001e.pdf.